

L-GALAXIES 2020: The evolution of radial metallicity profiles and global metallicities in disc galaxies

Robert M. Yates,^{1*} Bruno M. B. Henriques,² Jian Fu,³ Guinevere Kauffmann,¹ Peter A. Thomas,⁴

Qi Guo,⁵ Simon D. M. White¹ and Patricia Schady⁶

¹Max-Planck-Institut für Astrophysik, Karl-Schwarzschild-Straße 1, 85741, Garching, Germany

²Institute for Astronomy, ETH Zurich, CH-8093 Zurich, Switzerland

³Key Laboratory for Research in Galaxies and Cosmology, Shanghai Astronomical Observatory, CAS, 80 Nandan Road, Shanghai, 200030, China

⁴Astronomy Centre, University of Sussex, Falmer, Brighton BN1 9QH, UK

⁵Partner Group of the Max-Planck-Institut für Astrophysik, National Astronomical Observatories, Chinese Academy of Sciences, Beijing, 100012, China

⁶Department of Physics, University of Bath, Claverton Down, Bath, BA2 7AY, UK

Accepted XXX. Received YYY; in original form ZZZ

ABSTRACT

We present a modified version of the L-GALAXIES 2020 semi-analytic model of galaxy evolution, which includes significantly increased direct metal enrichment of the circumgalactic medium (CGM) by supernovae (SNe). These more metal-rich outflows do not require increased mass-loading factors, in contrast to some other galaxy evolution models. This modified L-GALAXIES 2020 model is able to simultaneously reproduce the gas-phase metallicity (Z_g) and stellar metallicity (Z_*) radial profiles observed in nearby disc galaxies by MaNGA and MUSE, as well as the observed mass – metallicity relations for gas and stars at $z = 0$ and their evolution back to $z \sim 2 - 3$. A direct CGM enrichment fraction of ~ 90 per cent for SNe-II is preferred. We find that massive disc galaxies have slightly flatter Z_g profiles than their lower-mass counterparts in L-GALAXIES 2020, due to more efficient enrichment of their outskirts via inside-out growth and metal-rich accretion. Such a weak, positive correlation between stellar mass and Z_g profile slope is also seen in our MaNGA-DR15 sample of 571 star-forming disc galaxies, although below $\log_{10}(M_*/M_\odot) \sim 10.0$ this observational result is strongly dependent on the metallicity diagnostic and morphological selection chosen. In addition, a lowered maximum SN-II progenitor mass of $25 M_\odot$, reflecting recent theoretical and observational estimates, can also provide a good match to observed Z_g and Z_* profiles at $z = 0$ in L-GALAXIES 2020. However, this model version fails to reproduce an evolution in Z_g at fixed mass over cosmic time, or the magnesium abundances observed in the intracluster medium (ICM).

Key words: methods: analytical – methods: data analysis – galaxies: abundances – galaxies: evolution

1 INTRODUCTION

The evolution of the metal content in and around galaxies remains a key area of contention in our understanding of galaxy evolution. On the observational side, discrepancies and uncertainties in metallicity measurements at both low and high redshift have led to conflicting interpretations for the interstellar medium (ISM) (e.g. Kewley & Dopita 2002; Yates et al. 2012; Sánchez et al. 2014; Belfiore et al. 2017; Erroz-Ferrer et al. 2019), stellar populations (e.g. Maraston 2005; Lonoce et al. 2020), and the circumgalactic medium (CGM) (e.g. Tumlinson et al. 2017; Werner & Mernier 2020; Péroux & Howk 2020). On the modelling side, degeneracies in the physical prescriptions implemented, and the tendency to focus on only a single galactic component or redshift, has hampered our ability to draw robust, definitive conclusions (e.g. Fu et al. 2012; Somerville et al. 2015; Somerville & Davé 2015; Collacchioni et al. 2018; Mitchell et al. 2020). Therefore, in order to make further progress in the field of galactic chemical evolution (GCE), we must look to combine accurate observational data from a range of phases and spatial scales with

detailed theoretical models that allow the simultaneous modelling of diverse galaxy populations.

To this end, we present a study of the L-GALAXIES 2020 semi-analytic model, which allows the self-consistent modelling of galaxies and their environments back to high redshift, including the internal evolution of their gas and stellar discs. This model is compared to a range of metallicity observations of the ISM, stars, CGM, and ICM, in order to more accurately constrain the relative importance of the various physical processes driving metallicity evolution in and around galaxies.

This paper is organised as follows: In Section 2, we introduce our modified L-GALAXIES 2020 model, and compare it to the default version presented in Henriques et al. (2020). In Section 3, we present the MaNGA sample used as our main low-redshift observational data set. In Section 4, we discuss the comparison between L-GALAXIES 2020 and various observations at low and high redshift, both for global metallicities and metallicity profiles. In Section 5, we contrast the findings from L-GALAXIES 2020 with those from other galaxy evolution models from the literature. In Section 6, we summarize our conclusions.

* E-mail: robbyates@mpa-garching.mpg.de

2 L-GALAXIES 2020

L-GALAXIES 2020 is a semi-analytic model of galaxy evolution, built to run on the dark matter (DM) subhalo merger trees of N-body simulations of cosmic structure formation. In this work, we apply L-GALAXIES 2020 to the merger trees from the $(480.3 \text{ Mpc}/h)^3$ MILLENNIUM and $(96.1 \text{ Mpc}/h)^3$ MILLENNIUM-II simulations (Springel et al. 2005; Boylan-Kolchin et al. 2009). This enables the study of millions of model galaxies in the mass range $7.0 \lesssim \log_{10}(M_*/M_\odot) \lesssim 12.0$, evolved from $z = 56$ to the present day in a *Planck-I* cosmology (see Angulo & White 2010; Angulo & Hilbert 2015).

This version of the L-GALAXIES model is the latest in a long line of major releases (e.g. Springel et al. 2001, 2005; De Lucia & Blaizot 2007; Guo et al. 2011; Henriques et al. 2015). The new model is discussed in detail in Henriques et al. (2020) and in the supplementary material available online.¹ Below, we give a brief overview of the key aspects most relevant to this work.

In addition to the existing implementations of gas cooling, SN feedback, AGN feedback, and other key processes, L-GALAXIES 2020 improves on the previous version of the model (Henriques et al. 2015) by including molecular hydrogen (H_2) formation (Fu et al. 2010), detailed chemical enrichment (Yates et al. 2013), and radially-resolved gas and stellar discs (Fu et al. 2013). This opens-up a whole new dimension of study into galaxy evolution, by allowing comparison to, and interpretation of, the latest observations of gas and stellar properties within galaxies from integral field units (IFUs).

In L-GALAXIES 2020, gas and stellar discs are divided into 12 concentric annuli (or ‘rings’) of fixed radius and width. As explained by Henriques et al. (2020, section 2.1), the outer edge of the i th ring is given by $r_i = 0.01 \cdot 2^i h^{-1} \text{ kpc}$, such that higher spatial resolution is obtained at lower radii. For our chosen cosmology, r_i ranges from 60.24 kpc for the outermost ring to 0.03 kpc for the innermost ring, meaning that L-GALAXIES 2020 resolves discs down to sub-kpc resolution in the centres of galaxies. The gas disc represents the cold interstellar medium (ISM) of galaxies, consisting of HII regions, atomic, and molecular gas. Material is allowed to flow between rings in the gas disc following a linear scaling between inflow velocity and radius, $v_{\text{inflow}} = \alpha_{\text{inflow}} r$, where α_{inflow} is the gas inflow parameter. Gas can also be expelled from discs via SN feedback occurring in each ring (see Section 2.1), and can cool onto the galaxy from the hot circumgalactic medium (CGM) at all radii. This accretion onto the disc is assumed to follow an exponential radial profile (see Henriques et al. 2020, section 2.2). The CGM in L-GALAXIES 2020, which encompasses all the hot gas surrounding a galaxy out to its virial radius (but not the material fully ejected out of the halo by feedback), is not spatially resolved. Consequently, the gas accreted onto discs is assumed to have a uniform metallicity. Likewise, the material within each ring in discs is assumed to be fully mixed, in qualitative agreement with observations of homogeneous azimuthal metal distributions within the ISM (e.g. Li et al. 2013; Kreckel et al. 2016, 2020).

The galactic chemical enrichment (GCE) scheme implemented into L-GALAXIES 2020 is explained by Henriques et al. (2020, section 2.4). In brief, the ages of AGB stars, SN-Ia progenitors, and SN-II progenitors from each stellar population formed are tracked, and their mass- and metallicity-dependent ejecta released into the ISM and CGM at the end of their lifetimes. The apportionment of this metal-rich material between the ISM and CGM is set by the model GCE parameters, which are discussed in the following section. The

yield tables used in L-GALAXIES 2020 are taken from Marigo (2001) for AGB stars, Thielemann et al. (2003) for SNe-Ia, and Portinari et al. (1998) for SNe-II. A power-law delay-time distribution (DTD) with a slope of -1.12 is assumed for SNe-Ia, following Maoz et al. (2012). The mass returned by SNe is used to calculate the amount of energy they deposit. This allows us to model a form of extended SN feedback in L-GALAXIES 2020, whereby stars from the same stellar population contribute to the reheating and ejection of gas at different times, depending on their mass- and metallicity-dependent lifetimes. This SN feedback scheme is discussed further in Sections 2.1.1 and 2.1.2 below.

H_2 formation in L-GALAXIES 2020 follows the gas partitioning scheme developed by Krumholz et al. (2009); McKee & Krumholz (2010). In this formalism, the H_2 mass fraction (μ_{H_2}) in the ISM depends on the local gas density and metallicity (see Henriques et al. 2020, section 2.2.3). Effectively, μ_{H_2} transitions from 0.0 at $\Sigma_{\text{ISM}} \lesssim 30 \text{ M}_\odot \text{pc}^{-2}$ to 1.0 at $\Sigma_{\text{ISM}} \gtrsim 100 \text{ M}_\odot \text{pc}^{-2}$, with only a weak secondary dependence on metallicity. The star-formation rate density in each ring in L-GALAXIES 2020 is then calculated from the local H_2 density and the DM subhalo dynamical time, $\Sigma_{\text{SFR}} = \alpha_{\text{SFR}} \Sigma_{\text{H}_2} / t_{\text{dyn}}$, where $\alpha_{\text{SFR}} = 0.06$ is the assumed dimensionless star formation efficiency (see Henriques et al. 2020, section 2.2.4). The α_{SFR} parameter, along with a number of other key physical parameters, is self-consistently constrained in L-GALAXIES 2020 using the Monte Carlo Markov Chain (MCMC) formalism developed by Henriques et al. (2009, 2015).

2.1 Modifications to the GCE parameters

The parameters controlling chemical enrichment in L-GALAXIES 2020 have been modified in this work to improve the correspondence with metallicity observations on global and sub-galactic scales.

The chief modification we make is to significantly increase the amount of material released by SNe which is allowed to directly enrich the CGM, without first mixing with the ambient ISM. This, along with the amount of direct CGM enrichment by AGB stars, is parameterised in the model by the $f_{\text{SNII,hot}}$, $f_{\text{SNIa,hot}}$, and $f_{\text{AGB,hot}}$ parameters (referred to collectively hereafter as the f_{hot} parameters).

Table 1 presents the values of the GCE parameters in both the default L-GALAXIES 2020 model presented in Henriques et al. (2020) (hereafter, the ‘default model’) and the ‘modified model’ introduced here. Both $f_{\text{SNII,hot}}$ and $f_{\text{SNIa,hot}}$ have been increased in the modified model to 90 and 80 per cent, respectively. This has been done to better match the normalisation of the gas-phase metallicity (Z_g) radial profiles seen in nearby galaxies (see Section 4.3), mimicking the metal-rich galactic outflows driven by SNe that are seen in star-forming galaxies both in observations (e.g. Martin et al. 2002; Strickland et al. 2004; Tumlinson et al. 2011) and hydrodynamical models (e.g. Gibson et al. 2013; Li et al. 2017; Emerick et al. 2020). Typically, SNe-Ia are assumed to pollute the hot CGM more efficiently than SNe-II. However, given that a significant fraction of SNe-Ia are also expected to explode promptly (see e.g. Yates et al. 2013; Maoz et al. 2014), and that much of the ejecta from SNe-II is expected to deposit into hot, low-density bubbles rather than cold, dense ISM, before outflowing (see e.g. Gatto et al. 2017), it is perhaps not so surprising that the values of $f_{\text{SNII,hot}}$ and $f_{\text{SNIa,hot}}$ required here are similar to each other. We find that values below ~ 75 per cent return gas and stellar metallicities in galaxies that are too high at $z = 0$, ISM metal enrichment rates that are too high at early times, and light α element abundances in the ICM that are too low by $z = 0$, compared to the observations considered in this work.

The $f_{\text{AGB,hot}}$ parameter has been increased only modestly to 25

¹ Supplementary material and model output catalogues from L-GALAXIES 2020 are available at <https://lgalaxiespublicrelease.github.io/>

GCE parameters	Default model	Modified model
$f_{\text{SNII,hot}}$	0.3	0.9
$f_{\text{SNIa,hot}}$	0.3	0.8
$f_{\text{AGB,hot}}$	0.0	0.25
A_{SNIa}	0.04	0.035
α_{inflow}	1.0	0.6

Table 1. The GCE parameter values chosen in L-GALAXIES 2020 for the default model presented in [Henriques et al. \(2020\)](#) and the modified model presented here. *Rows 1-3:* The fraction of material ejected by SNe-II, SNe-Ia, and AGB stars which is directly added to the hot CGM. *Row 4:* The fraction of stellar objects between 3 and 16 M_{\odot} in each stellar population that are assumed to be SN-Ia progenitor systems (see section 4 of [Yates et al. 2013](#)). *Row 5:* The gas inflow parameter (in $\text{km s}^{-1} \text{kpc}^{-1}$), which sets the speed of inflow within galaxy discs (see section 2.3.3 of [Fu et al. 2013](#)).

per cent in the modified model, in keeping with the expectation that AGB wind ejecta are predominantly released at low velocity and after SNe from the same generation of stars have exploded. More of the AGB ejecta material therefore remains available for immediate mixing with the cold ISM (see e.g. [Emerick et al. 2018](#)).

A significant increase in a unified f_{hot} parameter was also recommended by [Fu et al. \(2013\)](#) when studying the [Guo et al. \(2011\)](#) version of L-GALAXIES, in order to explain flat metallicity gradients in galaxies above $\log_{10}(M_*/M_{\odot}) \sim 10$. That version of the model did not contain the detailed GCE scheme ([Yates et al. 2013](#)) or improvements to gas reincorporation ([Henriques et al. 2015](#)) present in L-GALAXIES 2020, and was not compared to higher-redshift observational data or IFU data at low redshift.

The final two GCE parameters listed in Table 1 have a less significant impact on general galaxy evolution in L-GALAXIES 2020. The A_{SNIa} parameter, which represents the fraction of stellar objects of mass 3 – 16 M_{\odot} per stellar population which produce SNe-Ia, has been lowered slightly from 0.04 to 0.035. In combination with a ratio of $f_{\text{SNIa,hot}}/f_{\text{SNII,hot}} < 1$, this enables L-GALAXIES 2020 to maintain a good match to observations of the alpha enhancements in early-type galaxies (ETGs) at low redshift (see [Yates et al. 2013](#), section 6.3). This is necessary in response to the increase in the value of the f_{hot} parameters in the modified model. The gas inflow parameter, α_{inflow} , has also been lowered to 0.6 km/s/kpc , in order to slow the flow of gas into the centres of galaxies, reducing the amount of central star formation and hence helping to maintain the same HI mass function and central gas densities as seen in the default model (see Section 2.2). This produces inflow speeds of $< 5 \text{ km/s}$ in the inner $\sim 8 \text{ kpc}$ of galaxy discs, in good correspondence with high-resolution simulations of Milky-Way-sized galaxies ([Okalidis et al., in prep.](#)).

2.1.1 Reheating and ejection rates

Varying the f_{hot} parameters in L-GALAXIES 2020 not only changes the metal content in and around galaxies, but also the amount of energy available for gas reheating and ejection. As explained in section 2.4.1 of [Henriques et al. \(2020\)](#) and in more detail in section S1.10 of the supplementary material, the amount of energy available for reheating gas from the ISM to the CGM due to stellar feedback is given by

$$\Delta E_{\text{reheat}} = \min \left[\frac{1}{2} \epsilon_{\text{disc}} \Delta M_{\text{ret,ISM}} V_{\text{vir}}^2, \Delta E_{\text{SN,ISM}} \right], \quad (1)$$

where ϵ_{disc} is the reheating efficiency parameter,² V_{vir} is the virial velocity of the galaxy’s DM subhalo, $\Delta M_{\text{ret,ISM}}$ is the mass returned by SNe and stellar winds to the ISM, given by

$$\begin{aligned} \Delta M_{\text{ret,ISM}} = & (1 - f_{\text{SNII,hot}}) M_{\text{ret,SNII}} \\ & + (1 - f_{\text{SNIa,hot}}) M_{\text{ret,SNIa}} \\ & + (1 - f_{\text{AGB,hot}}) M_{\text{ret,AGB}}, \end{aligned} \quad (2)$$

and $\Delta E_{\text{SN,ISM}}$ is the total energy deposited into the ISM by SNe (also proportional to $\Delta M_{\text{ret,ISM}}$). We can therefore see that an increase in the f_{hot} parameters leads to a decrease in ΔE_{reheat} .

In turn, the total energy available for ejection of gas out of the CGM into an ejecta reservoir is given by

$$\Delta E_{\text{eject}} = \epsilon_{\text{halo}} (\Delta E_{\text{SN,ISM}} + \Delta E_{\text{SN,CGM}}) - \Delta E_{\text{reheat}}, \quad (3)$$

where ϵ_{halo} is the ejection efficiency parameter³ and $\Delta E_{\text{SN,CGM}}$ is the total energy deposited directly into the CGM by SNe, which depends on

$$\begin{aligned} \Delta M_{\text{ret,CGM}} = & f_{\text{SNII,hot}} M_{\text{ret,SNII}} \\ & + f_{\text{SNIa,hot}} M_{\text{ret,SNIa}} \\ & + f_{\text{AGB,hot}} M_{\text{ret,AGB}}. \end{aligned} \quad (4)$$

We can therefore see that the model partitions the total stellar feedback energy available between reheating ISM gas and ejecting CGM gas. Consequently, any reduction in the reheating energy leads to a complementary increase in the ejection energy. Even when the reheating energy is maximal (i.e. when $\Delta E_{\text{reheat}} = \Delta E_{\text{SN,ISM}}$), ΔE_{eject} can still be increased due to the dependence of $\Delta E_{\text{SN,CGM}}$ on the f_{hot} parameters.

Fig 1 illustrates this partitioning of SN energy in L-GALAXIES 2020 by showing the mean reheating and ejection rates for model star-forming galaxies of Milky-Way mass [$10.2 < \log_{10}(M_*/M_{\odot}) < 10.8$], selected at various redshifts. Red dashed lines represent the default model, and solid black lines and shaded regions represent the modified model. For the reheating rates, both components of galactic outflows are considered, namely (a) the SN ejecta itself and (b) the ambient ISM gas entrained in the SN-driven winds. We can see that the increased direct CGM enrichment in the modified model reduces the ISM reheating rate (top panel) by a factor of ~ 1.6 . In turn, the rate of ejection of hot gas out of the CGM (bottom panel) increases, because more energy is now available to drive outflows out of the subhalo.

The middle panel of Fig. 1 shows the reheating rate for metals only, again including both metals released from SNe and those entrained from the ISM. Metals are assumed to be fully mixed in each radial ring of the gas disc, so the entrained component of an outflow has the metallicity of this local ISM. This panel illustrates that more metal-rich galactic winds are present in the modified model, even though the *total* amount of material in these winds is actually lower (see top panel). This feature of the modified L-GALAXIES 2020 model distinguishes it from some other recent galaxy evolution models (see

² ϵ_{disc} can exceed 1.0 and acts in Eqn. 1 as a proportionality factor between the mass reheated by stellar feedback and the mass returned to the ISM by stars. It is dependent on the maximum rotation velocity of the subhalo, V_{max} , such that its value is typically larger in low-mass galaxies (see section S1.10 in the supplementary material).

³ ϵ_{halo} is simply the fraction of available SN energy that is allowed to couple with the CGM to drive outflows. It is effectively saturated at 1.0 for all subhaloes in L-GALAXIES 2020 (see section S1.10 in the supplementary material).

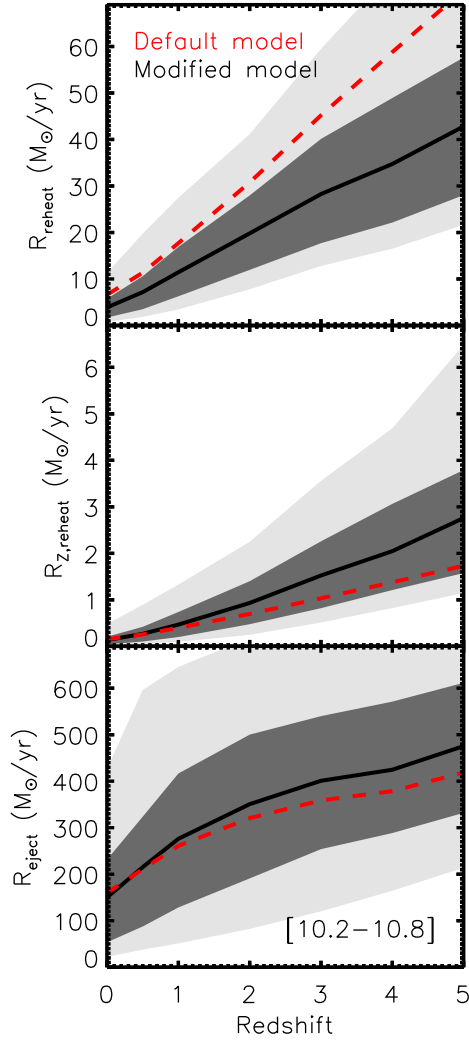


Figure 1. *Top panel:* The mean reheating rate of gas from the ISM into the CGM for star-forming galaxies with $10.2 < \log_{10}(M_*/M_\odot) < 10.8$ selected at various redshifts. *Middle panel:* The same as the top panel, but for metals only. *Bottom panel:* The mean ejection rate of gas from the CGM into an external ejecta reservoir. In all panels, dashed red lines denote the default model, and solid black lines denote the modified model. Dark and light grey regions represent the 16th–84th and 2nd–98th percentiles ranges for the modified model, respectively.

Section 5), and is also reflected in the mass-loading factors discussed in the following section.

2.1.2 Mass-loading factors

Although the values of the f_{hot} parameters are the same for galaxies of all masses in L-GALAXIES 2020, we note that the mass-loading factors for reheated and ejected material (i.e. $R_{\text{reheat}}/\text{SFR}$ and $R_{\text{eject}}/\text{SFR}$) are still weakly dependent on mass at $z = 0$. Fig. 2 shows $R_{\text{reheat}}/\text{SFR}$ as a function of M_{200} for all model galaxies at low redshift. The mass dependence seen is predominantly due to the inverse dependency of the reheating efficiency on V_{max} . Fig. 2 also illustrates how the amount of mass loading in the modified model is lower than in the default model, despite the increased metal ejection, as mentioned in the section above.

The reheating mass-loading factors as a function of mass in L-

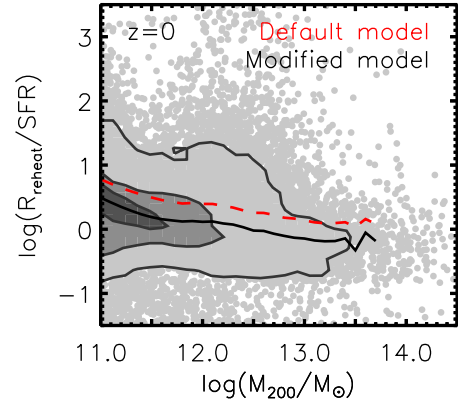


Figure 2. Mass-loading factors for reheated material as a function of M_{200} for all $z = 0$ galaxies with non-zero SFRs. Grey contours and points represent galaxies in the modified model. The red dashed and black solid lines represent the median relations from the default and modified models, respectively.

GALAXIES 2020 are in good agreement with those found by Mitchell et al. (2020) for the EAGLE hydrodynamical model. We note that, due to the incorporation of (a) delayed mass return from stars, and (b) non-zero direct enrichment of the CGM, the true mass-loading factors in L-GALAXIES 2020 are no longer simply equivalent to the ϵ_{disc} parameter. These mass-loading factors are also in good qualitative agreement with those calculated for observed quiescent galaxies at $z \sim 0.39 - 0.54$ by Leethochawalit et al. (2019).

2.2 General galaxy properties

The main results from L-GALAXIES 2020 concerning the general galaxy population were discussed in detail in Henriques et al. (2020). Here, we present some of the main relations again, to demonstrate that the changes to the GCE parameters discussed in Section 2.1 have not significantly altered the model’s match to its key observational constraints.

Fig. 3 shows a set of key galaxy relations from the L-GALAXIES 2020 model. In all panels, red lines represent the default model, black lines represent the modified model, and orange lines and points represent observational data. Solid lines show results when L-GALAXIES 2020 is run on the MILLENNIUM-I simulation, which produces well-resolved galaxies down to stellar masses of $\log_{10}(M_*/M_\odot) \sim 9.0$. Dashed lines show results when run on the higher-resolution MILLENNIUM-II simulation (Boylan-Kolchin et al. 2009), which allows us to more accurately probe lower-mass systems.

We can see from the left-hand panels that both versions of L-GALAXIES 2020 have very similar stellar mass functions (SMFs), reproducing the knee of the observed SMF at $z = 0$ and 2 reasonably well. At the high-mass end, both models are also in good agreement with the observed SMF measured by D’Souza et al. (2015) at $z = 0$, which accounts for the faint stellar light in the outskirts of massive elliptical galaxies and is therefore a closer match to the total stellar masses provided by L-GALAXIES 2020. We note that L-GALAXIES 2020 is not calibrated to this SMF, but rather to the combined SMFs at $z = 0 - 3$ shown by the solid orange lines (see Henriques et al. 2015, appendix A2).

The centre panels show the relation between stellar mass and specific star-formation rate (sSFR = SFR/M_*) for model galaxies at $z = 0$ and 2. They are illustrative of our finding that the ‘main

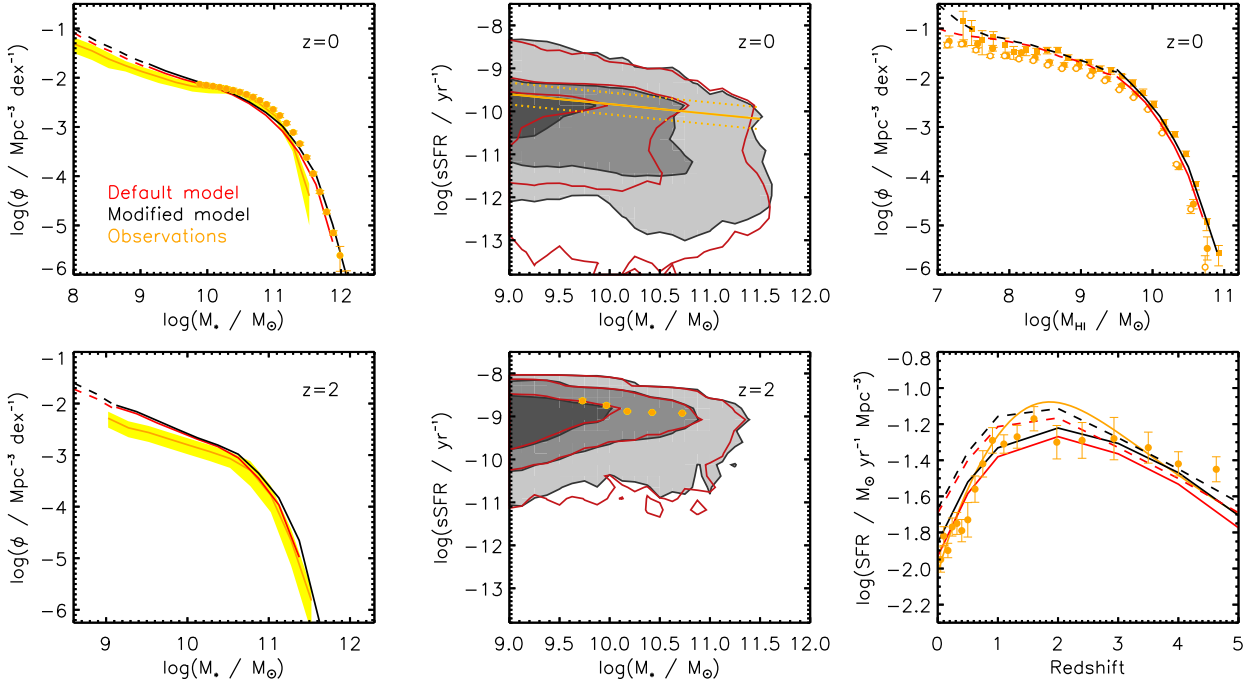


Figure 3. Key galaxy relations from the L-GALAXIES 2020 model. In all panels, red lines represent the default model, black lines represent the modified model, and orange lines and points represent observational data. Solid and dashed lines indicate models when run on the MILLENNIUM-I and MILLENNIUM-II simulations, respectively. *Top left panel:* The stellar mass function (SMF) for galaxies at $z = 0$. The observational data are from Baldry et al. (2008, 2012); Li & White (2009) (solid line), and D’Souza et al. (2015, filled circles). *Bottom left panel:* The SMF at $z = 2$. Observations are from the combined datasets discussed in appendix A2 of Henriques et al. 2015. *Top centre panel:* The M_* - sSFR relation for model galaxies, compared to a fit to star-forming systems from the SDSS-DR4 by Elbaz et al. (2007). *Bottom centre panel:* The M_* - sSFR relation at $z = 2$, compared to a dataset of 17 systems from the MOSDEF survey (Shivaei et al. 2016). *Top right panel:* The HI mass function (HIMF) at $z = 0$, compared to observational datasets from Zwaan et al. (2005, squares), Haynes et al. (2011, filled circles), and Jones et al. (2018, open circles). *Bottom right panel:* The evolution of the cosmic SFR density (SFRD) from $z = 5$ to $z = 0$, including observational relations from Madau & Dickinson (2014, orange line) and Driver et al. (2018, orange circles).

sequence’ of star-forming galaxies is very similar in the default and modified models at all redshifts. Likewise, the top right panel shows the HI mass function (HIMF) at $z = 0$, which is also similar in both models. This is because star-forming disc galaxies are able to compensate for the decreased reheating in the modified model by reducing their cooling rates, as these are predominantly determined by the amount of hot gas available. Such systems therefore maintain similar SFRs and total mass return rates in both models, reflecting the self-regulating nature of secularly-evolving, star-forming galaxies seen in equilibrium models (e.g. Bouché et al. 2010; Davé et al. 2012; Lilly et al. 2013).

The top-centre panel in Fig. 3 also shows a reduced spread of galaxies down to low sSFR in the modified model at low redshift, indicating higher overall SFRs in ‘red sequence’ galaxies (i.e. ETGs). This is also reflected in the cosmic star-formation rate density (SFRD), shown in the bottom-right panel, where the modified model exhibits a slightly higher SFRD than the default model. This change is due to slightly extended star-formation timescales in ETGs, caused by the reduced mass-loading factors and radial inflow speeds in the modified model compared to the default model. These changes bring the modified model into slightly better agreement with SFRD observations at high redshift, but slightly worse agreement at $z \sim 0$.

We can also see from the bottom-right panel that the SFRD evolution in both versions of L-GALAXIES 2020 is higher when run on MILLENNIUM-II than MILLENNIUM-I. As already discussed by Henriques et al. (2020), this is due to a combination of (a) the larger number of very-low-mass galaxies and (b) the higher typi-

cal SFRs in these systems when L-GALAXIES 2020 is run on the higher-resolution MILLENNIUM-II simulation. We note that, with the exception of Section 4.5, only MILLENNIUM-I runs are considered in the rest of this work, as we are interested in assessing the match between L-GALAXIES 2020 and observations of disc galaxies above $\log_{10}(M_*/M_\odot) \sim 9.0$.

We therefore conclude that the changes made in the modified L-GALAXIES 2020 model have a relatively negligible effect on the general global properties of galaxies, particularly the star-forming disc galaxies studied in this work. Given this, a full re-calibration of the model is not required, although we note that such a re-calibration, including the inclusion of the GCE parameters into the MCMC formalism (alongside a robust set of observational metallicity constraints), will be the focus of future work.

2.3 Model star-forming galaxy sample

In order to compare L-GALAXIES 2020 to the latest observational IFU data on the distribution of metals across disc galaxies (see Section 3), we require a sample of model systems that reflects the same mass range, morphology, and star-formation activity. Therefore, our model galaxy sample is formed by selecting systems with $\log_{10}(M_*/M_\odot) > 9.0$, $M_{\text{disc}}/(M_{\text{disc}} + M_{\text{bulge}}) > 0.7$, and $\log(\text{sSFR}/\text{yr}^{-1}) \geq \log_{10}[2 \cdot (1+z)^2/(t_{\text{H0}}/\text{yr})] - 1$, where t_{H0} is the Hubble time at $z = 0$. This last constraint selects galaxies with $\log(\text{sSFR}/\text{yr}^{-1}) \gtrsim -10.9$ at $z = 0$, increasing to $\gtrsim -9.7$ at $z = 3$ (see Henriques et al. 2020, appendix

A), and is found to accurately select the star-forming main sequence in both the default and modified model back to at least $z = 7$. This leaves us with $\sim 80,000$ galaxies at $z = 0$ in our star-forming model sample.

3 THE MANGA SAMPLE

In this work, we predominantly compare the low-redshift chemical properties of model galaxies to observational data from the Mapping Nearby Galaxies at the Apache Point Observatory (MaNGA) survey (Bundy et al. 2015). MaNGA obtains spatially-resolved maps out to 1.5 – 2.5 effective radii (R_e), by utilising the IFU and spectrograph mounted on the Sloan 2.5m optical telescope. Each MaNGA galaxy datacube is made up of spectra from a bundle of 19-127 fibres, providing a field-of-view of 12 – 32 arcsec (equivalent to 9.3 – 24.7 kpc at the median redshift of our MaNGA sample, $z \sim 0.037$).

Our MaNGA sample is drawn from SDSS data release (DR) 15. We utilise the derived data products from the MaNGA Data Analysis Pipeline (DAP) presented by Westfall et al. (2019) and Belfiore et al. (2019). This gives us access to Gaussian-profile integrated optical emission line fluxes and ancillary data for a base sample of 4,648 galaxies. We cross-match this base sample with the MaNGA FIREFLY v2.4.3 value-added catalogue (VAC) of 4,605 DR15 galaxies (Wilkinson et al. 2017; Goddard et al. 2017). This VAC provides absorption-line based stellar metallicities and ages, obtained using the FIREFLY spectral-fitting code which utilises the stellar population synthesis models of Maraston & Strömbäck (2011). This combination of emission-line and absorption-line data allows us to study both the gas and stellar properties in our sample galaxies from the same spectra. We take stellar masses from the NASA Sloan Atlas (NSA) v1.0.1⁴ (Blanton et al. 2011), which are fit to elliptical Petrosian fluxes. We have converted these stellar masses to our assumed cosmology (i.e. $h = 0.68$) by multiplying by a factor of $1/h^2 \sim 2.16$.

3.1 MaNGA sample selection

The MaNGA DAP provides emission-line information in two formats; individual spaxel spectra (the HYB10 datacubes), and co-added spectra for groups of spaxels (the VOR10 datacubes). When studying gas-phase (i.e. HII region) metallicities in MaNGA, we utilise the HYB10 spectra. This allows us to take advantage of their higher spatial resolution, noting that lower spatial resolution spectra can return erroneously flatten radial metallicity gradients (see e.g. Poetrodjojo et al. 2019; Acharyya et al. 2020). Because we are predominantly interested in azimuthally-averaged radial profiles and are measuring line ratios rather than absolute line fluxes, the leakage of light across HYB10 spaxels due to the large point spread function (PSF) in MaNGA should not be a significant issue (although, see Section 3.2).

In order to make a fair analysis of the radial metallicity profiles within galaxy discs, we restrict our MaNGA sample to systems with an inclination angle⁵ of $0^\circ \leq i < 60^\circ$, and which are identified as spiral galaxies in the Galaxy Zoo DR1 catalogue (Lintott et al. 2008, 2011) with a vote fraction of > 80 per cent. This reduces our sample to 663 systems, with the greatest reduction coming from the spiral

morphology requirement, which is found to hold for only 31 per cent of the full FIREFLY sample. This morphological requirement can have an important effect on the average Z_g profiles obtained for low-mass systems (see Section 4.4).

We also impose a cut on the global specific star-formation rate, selecting only galaxies with $\log(\text{sSFR}/\text{yr}^{-1}) \geq -11$, within errors. For this we utilised the total SFRs provided by the SDSS-DR7 catalogue (see Brinchmann et al. 2004; Salim et al. 2007) and the stellar masses provided by the NSA catalogue. We also only consider datacubes with a MaNGA DAP quality flag DAPQUAL of 0 (see Westfall et al. 2019, table 10) and spaxels/cells which fall within the MaNGA DAP quality mask.

For our Z_g analysis based on optical emission lines, we also require a minimum S/N of 3 on all lines used, and an equivalent width in the H α line of $\text{EW}(\text{H}\alpha) > 14\text{\AA}$. This latter criterion minimises the contamination by diffuse ionised gas (DIG, see e.g. Sanders et al. 2017; Lacerda et al. 2018). We also only select spectra which fall below the empirical demarcation line provided by Kauffmann et al. (2003) for the $[\text{NII}]/\text{H}\alpha - [\text{OIII}]/\text{H}\beta$ BPT diagram (Baldwin et al. 1981). This removes regions for which the ionising source is unlikely to be young stars, although we note that the clear majority of these regions are already removed by the $\text{EW}(\text{H}\alpha) > 14\text{\AA}$ cut. Finally, we correct all emission-line fluxes for internal dust extinction via the $\text{H}\alpha/\text{H}\beta$ ratio, using an intrinsic Balmer decrement of 2.86 and the Calzetti et al. (2000) attenuation law for star-forming galaxies, which assumes an extinction factor of $R'_V = 4.05 \pm 0.08$. We have checked that small changes to these selection criteria do not significantly affect our results. For example, while holding all other criteria fixed, varying the emission-line S/N threshold between 0 and 3, varying the $\text{EW}(\text{H}\alpha)$ threshold between 3 and 14\AA , and varying the maximum permitted inclination between 40 and 60° , does not alter the average metallicity profiles we obtain for each stellar mass bin.

The Z_* estimates calculated by FIREFLY utilise the VOR10 datacubes, which are formed by binning spaxels into ‘spatial cells’ to obtain $\text{S/N} \geq 10$ in the g -band continuum (Cappellari & Copin 2003). For our Z_* analysis, we select those VOR10 spatial cells with an uncertainty in their luminosity-weighted Z_* of less than 0.23 dex. This corresponds to an average S/N in the r -band of 5 (see Goddard et al. 2017, section 2.2). Following Goddard et al. 2017, we also only consider spatial cells within 1.5 effective radii (R_e), using the galactocentric radii normalised to the elliptical Petrosian r -band effective radius provided by the NSA catalogue.

These selection criteria leave us with a final MaNGA sample of 571 near-face-on disc galaxies, containing 450,635 spaxels with measurable Z_g (when using our preferred metallicity diagnostic, see below), and 272,975 spatial cells with measured Z_* from the FIREFLY catalogue.

3.2 Metallicity diagnostics

By far the biggest influence on the Z_g profiles we derive for our MaNGA sample comes from the choice of strong-line (SL) metallicity diagnostic. It is already well established that different SL diagnostics return a wide range of Z_g estimates, varying by up to 0.7 dex for the same spectra (Kewley & Ellison 2008). This has a significant impact on the scaling relations derived from samples of global spectra (e.g. Yates et al. 2012), and also affects the interpretation of galaxy radial metallicity profiles (e.g. Maiolino & Mannucci 2019).

Fig. 4 shows the mean radial Z_g profiles we obtain for our MaNGA sample when stacked by R/R_e , for four bins of stellar mass. Eight different SL Z_g diagnostics from the literature are considered: KD02-combi (Kewley & Dopita 2002), KK04-R23 (Kobulnicky & Kewley

⁴ <https://www.sdss.org/dr13/manga/manga-target-selection/nsa/>

⁵ Following Giovanelli et al. (1994), we assume an ‘intrinsic ellipticity’ (caused by an intrinsic disc thickness) of $q_{\text{el}} = 0.13$ when calculating the inclination angle from the observed axial ratios (b/a) provided by the NSA catalogue, where $\cos^2 i = [(b/a)^2 - q_{\text{el}}^2] / (1 - q_{\text{el}}^2)$.

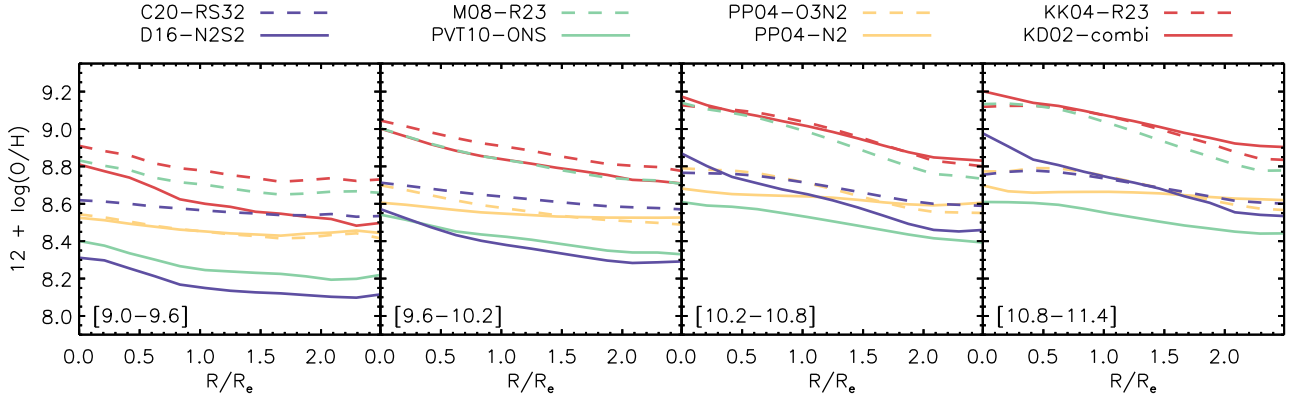


Figure 4. Gas-phase metallicity (Z_g) profiles as a function of R/R_e from our MaNGA sample, split into four bins of stellar mass. Z_g is calculated using the following eight strong line (SL) metallicity diagnostics from the literature: Dashed blue lines, $[\text{OIII}]/\text{H}\beta + [\text{SII}]/\text{H}\alpha$ from Curti et al. (2020, C20-RS32); solid blue lines, $[\text{NII}]/[\text{SII}] + [\text{NII}]/\text{H}\alpha$ from Dopita et al. (2016, D16-N2S2); dashed green lines, $([\text{OIII}]+[\text{OII}])/\text{H}\beta$ from Maiolino et al. (2008, M08-R23); solid green lines the oxygen-nitrogen-sulphur combined diagnostic from Pilyugin et al. (2010, PVT10-ONS); dashed orange lines, $[\text{OIII}]/[\text{NII}]$ from Pettini & Pagel (2004, PP04-O3N2); solid orange lines, $[\text{NII}]/\text{H}\alpha$ from Pettini & Pagel (2004, PP04-N2); dashed red lines, $([\text{OIII}]+[\text{OII}])/\text{H}\beta$ from Kobulnicky & Kewley (2004, KK04-R23) which includes an iterative q correction using $[\text{OIII}]/[\text{OII}]$; and solid red lines, the combined diagnostic proposed by Kewley & Dopita (2002, KD02-combi) which utilises $[\text{NII}]/[\text{OII}]$ for metallicities above 8.6 dex.

2004), PP04-N2 & PP04-O3N2 (Pettini & Pagel 2004), M08-R23 (Maiolino et al. 2008), PVT10-ONS (Pilyugin et al. 2010), D16-N2S2 (Dopita et al. 2016), and C20-RS32 (Curti et al. 2020a). These diagnostics have been chosen to represent a range of different emission-line ratios and calibration samples.

The first noticeable feature in Fig. 4 is the large difference in normalisation between the profiles at fixed mass. The variation of up to ~ 0.6 dex seen here is reminiscent of that seen for the global MZ_gR when using different SL diagnostics (Kewley & Ellison 2008), and is arguably more significant than the variation in slope (although see Section 4.4). The second noticeable feature is the large difference in mass dependence between the different SL diagnostics. Some suggest a large increase in Z_g profile normalisation with stellar mass (e.g. KD02-combi, D16-N2S2), whereas others suggest essentially no change in metallicity with mass at all (e.g. PP04-N2, C20-RS32).

As shown by Yates et al. 2020 and others, SL diagnostics which return a low Z_g at low mass (e.g. PVT10-ONS and D16-N2S2) are in better agreement with metallicities obtained from a variety of direct methods, such as metal recombination lines (Esteban et al. 2009, 2014), absorption lines from blue supergiant photospheres (Kudritzki et al. 2016), and electron temperature (T_e) measurements (e.g. Bresolin et al. 2009). Such methods are typically considered more accurate than SL diagnostics in low-metallicity environments (e.g. Bresolin 2008). The other SL diagnostics considered here, particularly KD02-combi and M08-R23, predict global metallicities at low mass which are higher than expected from direct measurements by up to ~ 0.45 dex.

At higher masses, the PVT10-ONS diagnostic returns particularly low Z_g estimates, predicting that star-forming disc galaxies with $\log_{10}(M_*/M_\odot) \sim 11.5$ should have sub-solar ISM metallicities at all radii. Similarly, the PP04-N2 diagnostic is known to saturate at around solar metallicity, prohibiting its use for the highest-mass systems (see e.g. Kewley & Dopita 2002). On the other hand, the D16-N2S2 diagnostic returns high Z_g at high mass, predicting super-solar ISM metallicities within $\sim 1 R_e$ at Milky-Way masses and above.

Another interesting feature seen in Fig. 4 is the differences in inner slope exhibited by different SL diagnostics for massive galaxies (see

also Boardman et al. 2020). Those diagnostics which rely on $[\text{OIII}]$ lines (i.e. KK04-R23, PP04-O3N2, M08-R23, PVT10-ONS, C20-RS32) all suggest a flattening within $\sim 0.5 R_e$ at $\log(M_*/M_\odot) \geq 10.2$ (i.e. the two highest-mass bins), whereas those which do not (i.e. KD02-combi, PP04-N2, D16-N2S2) suggest a continued increase in metallicity towards the centre.

We note that Belfiore et al. (2017) caution against drawing physical conclusions from metallicity gradients within $\sim 0.5 R_e$ in MaNGA, due to the beam-smearing effects caused by high PSF/R_e values. This can lead to a slight but systematic flattening of measured Z_g profiles in the inner regions of galaxies. Inclination effects can also contribute in this respect (Belfiore et al. 2017), and physical effects such as radial gas motions could also play a role (Sánchez et al. 2014). Nonetheless, the fact that the SL diagnostics considered here exhibit strong and *diverse* changes to the inner slope suggests that diagnostic-specific biases should also be considered.

A common candidate for such SL diagnostic biases is a dependence on the ionisation state of the line-emitting gas. This is typically represented by the ionisation parameter, $q = S(\text{H}^0)/n_H$, which is the ratio of the ionising photon flux density to the electron density and describes the speed of propagation of an ionising front through hydrogen. Fig. 5 shows the radial q profiles for our MaNGA sample, using five different SL q diagnostics. The $[\text{OIII}]/[\text{OII}]$ and $[\text{NIII}]/[\text{OII}]$ ratios used for most of these are themselves dependent on metallicity, so we have corrected them using the SL Z_g diagnostics described above. We find that the q profiles obtained are the same regardless of which SL Z_g diagnostic is used for this correction.

Fig. 5 shows evidence of a clear increase in q towards the centres of massive galaxies. This can affect the Z_g profiles returned by SL Z_g diagnostics which have a secondary dependence on q . For example, the O3N2 ratio is known to have a strong positive dependence on q (e.g. Kewley & Dopita 2002). Therefore, O3N2 diagnostics calibrated to samples exhibiting a strong one-to-one anti-correlation between q and Z_g (likely the case for most empirical HII region samples) would under-predict the true metallicity for high- q regions. This could partly explain the flattened inner profile returned by diagnostics such as PP04-O3N2 in Fig. 4. However, this is not necessarily the case for other SL diagnostics which return flattened inner pro-

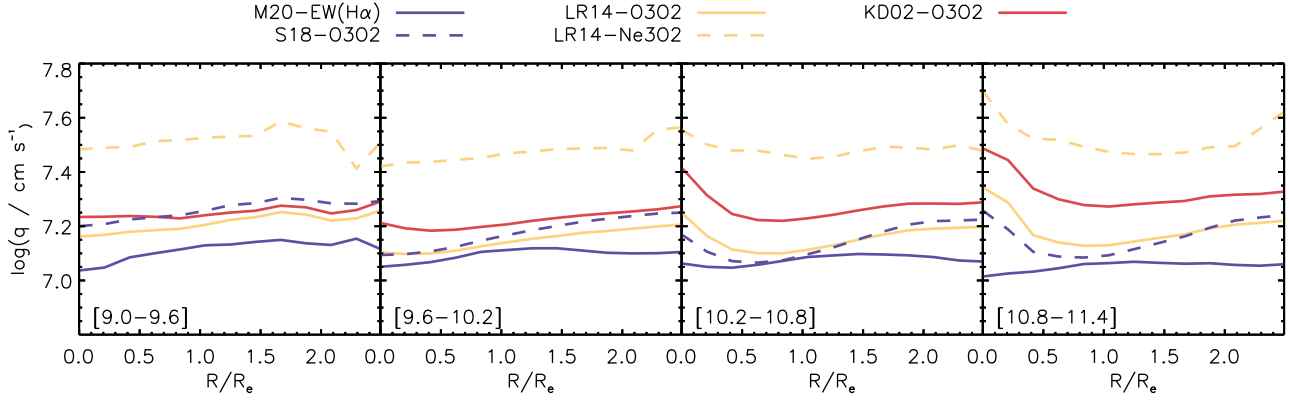


Figure 5. Ionisation parameter (q) profiles as a function of R/R_e for our MaNGA sample, split into four mass bins. Profiles are obtained using the following five SL q diagnostics: M20-EW($H\alpha$) (Mingozzi et al. 2020, solid blue lines), S18-O3O2 (Strom et al. 2018, dashed blue lines), LR14-O3O2 (Levesque & Richardson 2014, solid orange lines), LR14-Ne3O2 (Levesque & Richardson 2014, dashed orange lines), KD02-O3O2 (Kewley & Dopita 2002, solid red lines).

files. For example, the KK04-R23 diagnostic, which has a negative q dependence and iteratively corrects for this while solving for Z_g , also returns a flattened profile at low radii in massive galaxies.

We therefore conclude that q dependencies could affect the observed inner Z_g profile in high-mass galaxies, but the nature of this affect is complex and likely dependent on the line ratio and calibration sample used. Consequently, we recommend the use of SL diagnostics which do not have a strong q dependence, in order to avoid such issues. Further investigation using metallicity-independent q diagnostics, direct measurements of Z_g , and a wider range of spatial scales is required in order to draw more comprehensive conclusions (see Easeman et al., in prep.).

Given the arguments above, in this work we choose to adopt the D16-N2S2 diagnostic when estimating MaNGA gas-phase metallicities in this work. This diagnostic is well matched in normalisation to direct metallicity measurements at low mass (see Section 4.1.1), predicts super-solar Z_g in very massive galaxies, has a relatively negligible dependence on q , and is also calibrated assuming the observed O/H – N/O relation obtained from direct measurements of stellar and HII-region spectra (see Dopita et al. 2016, section 4.2). This last factor is important given the use of the [NII] λ 6584 line in this diagnostic when estimating the oxygen abundance.

Nonetheless, we note that, like the SL ratios used in some other common diagnostics (e.g. N2 and O3N2), the [NII]/[SI] and [NII]/ $H\alpha$ ratios used in the D16-N2S2 diagnostic do not directly contain a measurement of collisionally-excited oxygen lines to hydrogen recombination lines. This diagnostic instead relies on a good correspondence between the assumed O/H – N/O relation and that of the particular sample studied. The position of a galaxy on the O/H – N/O relation can depend on its M_* and SFR (e.g. Andrews & Martini 2013), and more generally on the evolutionary stage of the galaxy (e.g. Vincenzo et al. 2016). In our case, the O/H – N/O relation for our MaNGA sample is relatively tight and its slope is in good qualitative agreement with that expected by Dopita et al. (2016), when considering a number of different SL N/O and O/H diagnostics. The metallicity profiles we present are also averages in bins of stellar mass, and we note that Andrews & Martini (2013) find galaxies stacked by mass return a tight and consistent O/H-N/O trend. Therefore, we do not expect biases due to deviations in the star formation histories among our sample to be significant here.

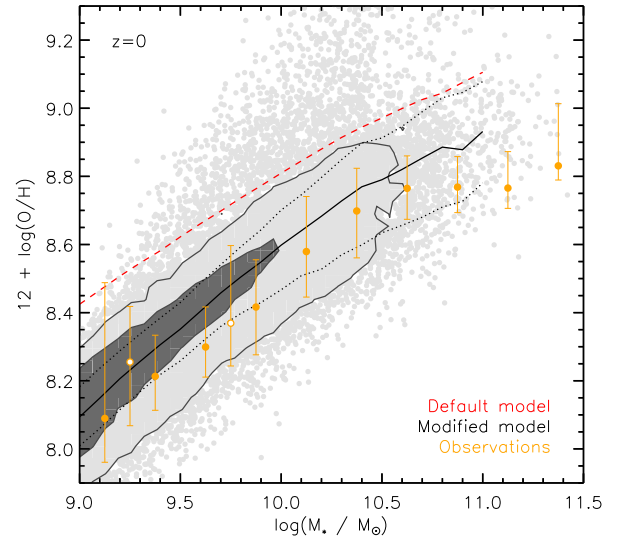


Figure 6. The relation between stellar mass and SFR-weighted gas-phase metallicity (the MZ_gR) for star-forming galaxies at $z = 0$. Contours denote the 1σ and 2σ distributions for the modified L-GALAXIES 2020 model, the solid black line denotes the mean relation, and the dotted black lines denote the 16th and 84th percentiles. The mean relation from the default model is shown as a red dashed line. The two observed binned MZ_gRs also shown are from T_e -based metallicity measurements made by Yates et al. (2020, open orange circles), and strong-line metallicities using the D16-N2S2 diagnostic for the MaNGA sample presented in Section 3 (orange circles).

4 RESULTS

Before discussing radial profiles, we first present the global metallicities present in the ISM, stars, CGM, and ICM at low redshift, and discuss their evolution over cosmic time.

4.1 Global metallicities at low redshift

4.1.1 ISM metallicities at low redshift

Fig. 6 shows the relation between stellar mass and ISM metallicity (the MZ_gR) at $z = 0$ for star-forming, disc-dominant galaxies. Model galaxies from the modified model are represented by grey contours

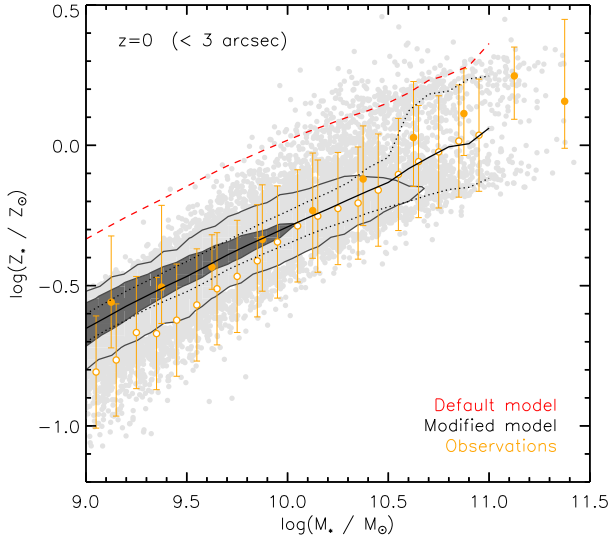


Figure 7. The relation between stellar mass and mass-weighted stellar metallicity (the MZ_{*R}) within 3 arcsec for star-forming galaxies at $z = 0$. Lines, contours, and colours are as in Fig. 6. The two observed MZ_{*R} s shown are from Zahid et al. (2017, open orange circles) and our MaNGA sample presented in Section 3 (filled orange circles).

and points. The mean relation for the modified model (black, solid line) and the default model (red, dashed line) are also shown. In order to best mimic observations, global Z_g in L-GALAXIES 2020 is obtained by first calculating the local Z_g within each radial ring in units of $12 + \log(O/H)$,⁶ and then taking the SFR-weighted mean of these local values.

The observational MZ_gR from our MaNGA sample is also shown as filled orange circles, with the vertical error bars representing the 1σ spread in Z_g in each mass bin. This is formed by calculating the global $H\alpha$ -flux-weighted Z_g (using the D16-N2S2 SL diagnostic, see Section 3.2) for each MaNGA galaxy, and plotting the mean of these global metallicities in 0.25 dex wide bins of stellar mass. The upper end of the MZ_gR , derived from galaxies with T_e -based Z_g measurements (Yates et al. 2020), is also shown (open orange circles). We can see a good agreement between the D16-N2S2-based and T_e -based MZ_gR s, as discussed in Section 3.2.

The MZ_gR from the modified model agrees well with the observations shown in Fig. 6. The decrease in normalisation compared to the default model is due to the reduction in metal enrichment of the ISM that occurs when the f_{hot} parameters are increased.

We also find that, at $\log_{10}(M_*/M_\odot) \lesssim 10.2$, both the default and modified models reproduce an anti-correlation between SFR and Z_g at fixed mass, as expected from the fundamental metallicity relation (FMR, Mannucci et al. 2010). At higher mass, this SFR- Z_g trend is reversed in the modified model (as seen in previous versions of L-GALAXIES and some observations, Yates et al. 2012), but not in the default model. This difference is likely due to the more significant impact that increased metal removal has on low-SFR massive galaxies in our model galaxy sample. This is an interesting finding which we intend to investigate further in future work.

We note that the default L-GALAXIES 2020 model better matches the MZ_gR s inferred from theoretically-calibrated $[OIII]$ -based SL di-

agnostics, such as those from Kewley & Dopita (2002) and Maiolino et al. (2008) (see Henriques et al. 2020, fig. 13). However, unlike the D16-N2S2 diagnostic chosen in this work, those SL diagnostics are inconsistent with direct Z_g measurements for low-mass galaxies and HII regions (see Section 3.2). Higher ISM metallicities in the default model also lead to a much reduced evolution in the MZ_gR back to high redshift, which is discussed further in Section 4.2.

4.1.2 Stellar metallicities at low redshift

Fig. 7 shows the relation between stellar mass and stellar metallicity (the MZ_{*R}) at $z = 0$ for star-forming, disc-dominant galaxies. To calculate global stellar metallicities in L-GALAXIES 2020, we first measure the solar-normalised metal-to-total stellar mass ratio in each radial ring, $\log(Z_*/Z_\odot) = \log_{10}(M_{*,Z}/M_*) - \log_{10}(Z_\odot)$, where $Z_\odot = 0.0142$ is the metallicity in the bulk of the Sun (Asplund et al. 2009), and then take the stellar-mass-weighted mean as the global Z_* .

The observational MZ_{*R} s for low-redshift galaxies plotted in Fig. 7 come from two sources, (a) mass-weighted, central Z_* measurements from our MaNGA sample provided by the FIREFLY catalogue (filled orange circles), and (b) mass-weighted, central Z_* measurements from absorption lines in stacked spectra of $\sim 200,000$ SDSS-DR7 star-forming galaxies from Zahid et al. (2017) (open orange circles). We have assigned a nominal uncertainty of 0.2 dex to the Zahid et al. (2017) binned data, given that their complimentary luminosity-weighted metallicities are expected to be accurate to within ~ 0.1 dex, with the uncertainty in the mass-weighted counterparts being larger due to additional dependencies on the assumed star formation history (H. J. Zahid, priv. comm.).

All observational Z_* measurements used in Fig. 7 have been obtained within a 3 arcsec aperture – the diameter of an SDSS fibre. This equates to 2.29 kpc at the median redshift of our MaNGA sample ($\bar{z} = 0.037$). At low redshifts, such limited apertures can return significantly higher Z_* estimates, due to the presence of negative metallicity gradients in galaxies (see e.g. Okamoto et al. 2017). Therefore, we measure global Z_* for our model galaxies only within the innermost 7 rings for Fig. 7, equating to a diameter of 1.88 kpc, in order to better compare with observations. This increases the mean Z_* by ~ 0.12 dex at all masses in the model. Interestingly, this aperture ‘anti-correction’ also reduces the 1σ spread in Z_* by ~ 0.05 dex at low mass, indicating that variations among galaxies’ Z_* at larger radii could be an important component of the scatter in the MZ_{*R} .

A key result of this work is that the modified L-GALAXIES 2020 model is able to simultaneously reproduce both the MZ_gR and MZ_{*R} at $z = 0$. The improved agreement here is due to the improved accuracy and precision of the observational data considered, the choice of Z_g diagnostic used, and the significant decrease in ISM enrichment efficiency in the modified model compared to the default model.

4.1.3 CGM metallicities at low redshift

It is important to also consider the metal content in the hot gas surrounding galaxies, particularly given that our modified model significantly increases the efficiency with which SNe can directly pollute the CGM.

Fig. 8 shows the relation between stellar mass and CGM metallicity (excluding ejected material beyond R_{vir}) for star-forming, disc-dominant galaxies at $z = 0.22$. Model metallicities are measured as $\log_{10}(Z_h/Z_\odot) = \log_{10}(M_{h,Z}/M_h) - \log_{10}(Z_\odot)$, where

⁶ Where O/H is the ratio of the number density of oxygen atoms to hydrogen atoms in the gas.

$Z_{\odot} = 0.0134$ is the solar photospheric metallicity from [Asplund et al. \(2009\)](#) assumed in the observations to which we compare here.

The observational data shown in Fig. 8 is taken from the re-analysis by [Prochaska et al. \(2017\)](#) of absorption-line-based metallicities from the COS-Halos Survey ([Tumlinson et al. 2011, 2017](#)). These metallicities were obtained via Cloudy ([Ferland et al. 2013](#)) modelling of Si^+ and Si^{++} absorption lines, assuming solar relative abundances from [Asplund et al. \(2009\)](#) and a [Haardt & Madau \(2012\)](#) EUVB radiation field. We have corrected the stellar masses and SFRs from the COS-Halos sample (provided by [Werk et al. 2012](#)) to assume a [Chabrier \(2003\)](#) IMF and our value of $h = 0.68$, and have selected only systems with $\log_{10}(\text{sSFR}/\text{yr}^{-1}) > -11$ and 1σ uncertainties in Z_h of < 0.5 dex. This leaves 16 systems with $\bar{z} = 0.22$ and a median impact parameter of 64 kpc. This observational data set has then been split into two sub-samples: (a) ‘low-density systems’ with $15.0 < \log_{10}(N_{\text{HI}}/\text{cm}^{-2}) < 17.2$ (filled orange circles) which are optically thin to ionizing radiation and directly trace the hot CGM, and (b) ‘Lyman limit systems (LLSs)’ with $17.2 < \log_{10}(N_{\text{HI}}/\text{cm}^{-2}) < 19.0$ (open orange circles) which are found in simulations to have neutral gas fractions of $\sim 10^{-2}$ and typically reside close to galaxies (see [Péroux & Howk 2020](#), section 1.2). It is the low-density systems which provide the best comparison to the CGM modelled in L-GALAXIES 2020, which is considered to contain hot, non-star-forming gas extending out to the virial radius.

The scatter in the observational data in Fig. 8 is considerably larger than that seen in L-GALAXIES 2020. This could be partly due to variations in the impact parameter on the observational side, and the flat metallicity gradients assumed for the CGM on the model side. However, as also found by [Prochaska et al. \(2017\)](#), we find no trend in Z_h with impact parameter (even at fixed mass) for the COS-Halos data, suggesting that inner metallicity gradients are not systematically present in the CGM of star-forming galaxies.

The mean Z_h for the COS-Halos low-density systems is $Z_h/Z_{\odot} = -0.25$, which can be compared to $Z_h/Z_{\odot} = -0.24$ for the default L-GALAXIES 2020 model and $Z_h/Z_{\odot} = -0.13$ for the modified model at the same mean stellar mass of $\log_{10}(M_*/M_{\odot}) \sim 10.1$. This suggests that there is a slight over-abundance of metals in the CGM for the modified model compared to observations. However, we note that this excess metal is predominantly in light α elements, which are most efficiently driven out of galaxies by prompt SNe-II (see [Yates et al. 2013](#)). Heavier α elements, such as silicon, have more similar CGM abundances in our default and modified models, with a difference in $[\text{Si}/\text{H}]$ of only ~ 0.06 dex at the same redshift and mass. Therefore, observational analyses that focus only on heavier alpha elements and assume solar relative abundances could underestimate the overall Z_h in the CGM (see also [Wotta et al. 2019](#)). Nonetheless, this comparison with COS-Halos data suggests that the value of $f_{\text{SNI,hot}} = 0.9$ used in the modified model is close to its maximum permissible value.

4.1.4 IGrM and ICM metallicities at low redshift

In higher-temperature systems, such as galaxy groups and clusters,⁷ emission lines from key metal ions such as iron become prominent in X-ray spectra, allowing for more precise measurements of the metal abundance to be made.

Fig. 9 shows the mass-weighted chemical abundances of Mg, Si, S, and Fe in the intra-group medium (IGrM) and ICM, as a function

⁷ defined as systems with $13 \lesssim \log(M_{\text{vir}}/M_{\odot}) \lesssim 14$, and $\log(M_{\text{vir}}/M_{\odot}) \gtrsim 14$, respectively.

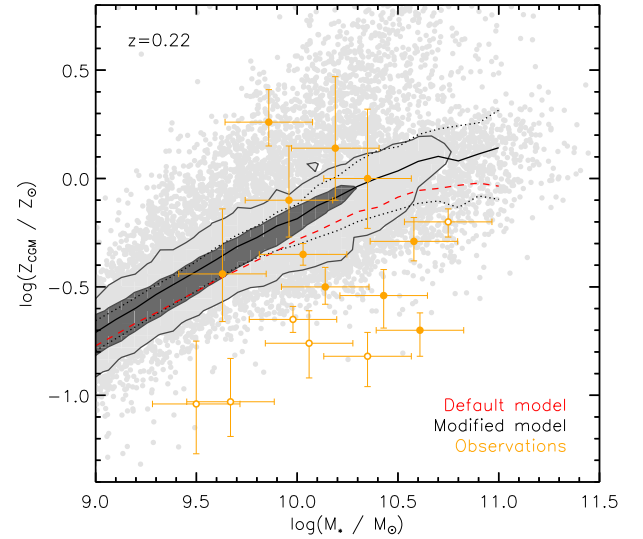


Figure 8. The relation between stellar mass and total metallicity in the CGM (the MZ_hR) for star-forming galaxies at $z = 0.22$. Lines, contours, and colours are as in Fig. 6. The observations shown here are taken from the COS-Halos Survey ([Tumlinson et al. 2011](#); [Prochaska et al. 2017](#)): filled orange circles denote ‘low-density systems’, and open orange circles denote ‘Lyman limit systems’ (LLSs).

of the temperature at r_{500} (i.e. the TZ_{ICMR}). The mean relations for the default model (red) and modified model (black) are shown, along with the mean relation for the MaxGCEMass25 model (blue) discussed in Section 4.6.2. A compilation of observational data from [Yates et al. \(2017\)](#) (open orange circles) and [Mernier et al. \(2018a,b\)](#) (filled orange circles) are also shown, along with the recent measurement of the iron abundance in the Perseus cluster from *Hitomi* by [Simionescu et al. \(2019\)](#) (white-edged square). Here, radial gradients in temperature, gas density, and metallicity are accounted for, with both model and observational data being homogenised and re-scaled to r_{500} following the techniques presented in [Yates et al. \(2017\)](#) and updated in section 4.1.3 of [Henriques et al. \(2020\)](#).

Fig. 9 shows that the modified model matches well to the chemical abundances observed in the IGrM and ICM for all four elements considered here. The higher abundances seen compared to the default model are again due to the increased direct CGM enrichment by SNe-II and SNe-Ia. We note that most significance should be given to the $[\text{Si}/\text{H}]$, $[\text{S}/\text{H}]$, and $[\text{Fe}/\text{H}]$ abundances here, as Mg measurements from X-ray spectra can be significantly affected by both background and instrumental effects beyond the core region (F. Mernier, priv. comm.). In order to minimise such biases, we have adopted the shape parameters (x_c and α) obtained from the beta-profile fit to the $[\text{Fe}/\text{H}]$ profile when re-scaling $[\text{Mg}/\text{H}]$ here, while still allowing the normalisation to remain free (see [Yates et al. 2017](#), section 2.4). Nonetheless, we advise caution when comparing Mg abundances between models and observations.

From Fig. 9 we conclude that the modified L-GALAXIES 2020 model does even better than the default model in reproducing the typical metal content seen in the hot gas surrounding groups and clusters at $z = 0$. This is a further indication that the increased direct CGM enrichment implemented in the modified model works well for metallicities both inside and outside galaxies.

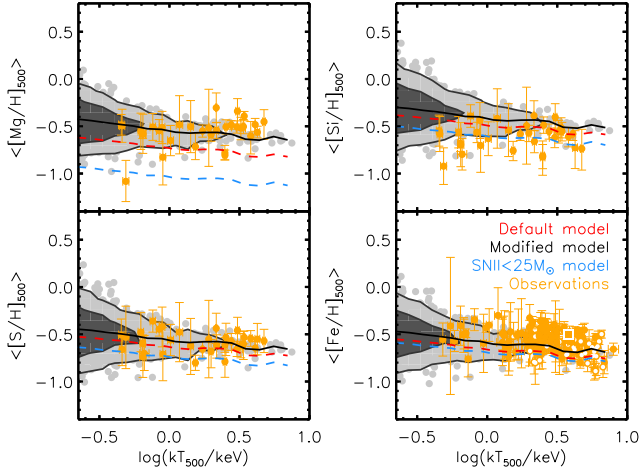


Figure 9. The relation between temperature at r_{500} and the mean abundance within r_{500} of [Mg/H], [Si/H], [S/H], and [Fe/H] in the ICM (i.e. the TZ_{ICMR}). Grey contours denote systems from the modified L-GALAXIES 2020 model, with the mean relation given by the black solid lines. The mean relation for the default model (red dashed lines) and MaxGCEMass25 model (blue dashed lines) are also shown. Observational data include: homogenised [Fe/H] measurements for clusters from Yates et al. (2017) (open orange circles), abundances for all four chemical elements from the CHEERS sample (Mernier et al. 2018a,b) (filled orange circles), and the [Fe/H] measured by *Hitomi* for the Perseus cluster (Simionescu et al. 2019) (white-edged square).

4.2 Evolution of global metallicities

The top panel of Fig. 10 shows the evolution of the MZ_gR for the modified model from $z = 5$ to the present day. This model exhibits a clear increase in Z_g at fixed stellar mass over cosmic time, caused by the efficient removal of newly-formed metals out of galaxies. In contrast, our default model exhibits a negligible evolution in Z_g at high mass, and even a mildly *inverted* evolution at low mass, due to an over-enrichment of the ISM at early times. Such issues have been common to older galaxy evolution models (see e.g. Yates et al. 2012; Fu et al. 2012; Guo et al. 2016; Knebe et al. 2018), particularly those which do not calibrate to higher-redshift observational data (D. Stoppacher, priv. comm.).

For the modified model, we find an increase in mean Z_g between $z = 3$ and 0 at $\log_{10}(M_*/M_\odot) = 10.0$ of ~ 0.3 dex. This is in good agreement with other semi-analytic and hydrodynamical models, which find a typical evolution in Z_g of 0.25 - 0.45 dex for the same redshift range and stellar mass (e.g. ILLUSTRIS, Torrey et al. 2014; SANTA CRUZ, Somerville et al. 2015; GAEA, Hirschmann et al. 2016; FIRE, Ma et al. 2016; MUFASA, Davé et al. 2017; EAGLE, De Rossi et al. 2017; SAG, Collacchioni et al. 2018; SIMBA, Davé et al. 2019; ILLUSTRIS-TNG, Torrey et al. 2019). However, some of these theoretical studies rely on explicit redshift dependencies to drive an increase in the normalisation of the MZ_gR over cosmic time. The modified L-GALAXIES 2020 model, on the other hand, is able to reproduce a clear evolution in Z_g at fixed mass by using a standard V_{max} -dependent reheating efficiency and a large, fixed direct CGM enrichment efficiency.

Fig. 11 shows the evolution of Z_g for the modified model in comparison to various observational studies at different redshifts. This comparison is made for a fixed stellar mass bin of $9.0 \leq \log_{10}(M_*/M_\odot) < 10.0$, to mitigate the strong dependence on stellar

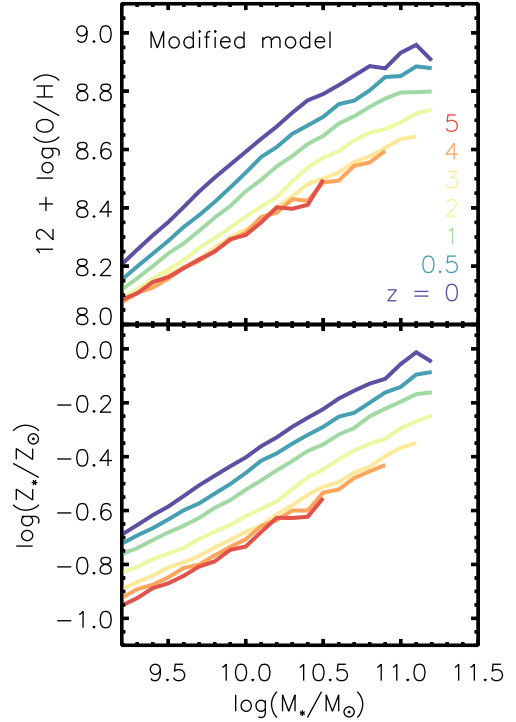


Figure 10. Evolution of the MZ_gR (top panel) and MZ_*R (bottom panel) from redshift 5 to 0 in the modified L-GALAXIES 2020 model for model galaxies selected at each redshift to be star-forming and disc-dominant.

mass that both metallicity and detectability can have. The modified L-GALAXIES 2020 model is shown by black solid lines, which bracket the range of *mean* Z_g present in galaxies within our chosen mass range. The same range for the default model is shown by red dashed lines.

The equivalent range of Z_g from three different observational studies utilising SL Z_g diagnostics are also shown: Maiolino et al. (2008) (grey shaded region, using a combination of KD02-combi, M08-O3, and M08-N2), Zahid et al. (2014) (blue shaded region, using KK04-R23 and PP04-N2), and Hunt et al. (2016) (yellow shaded region, using various diagnostics re-scaled to PP04-N2). Our MaNGA sample at $z \sim 0.037$ is also shown by the orange bar, offset to negative redshift in Fig. 11 for clarity. Finally, a small collection of galaxies within the chosen mass range with directly-measured ISM metallicities are also shown: galaxies with electron-temperature based Z_g from Yates et al. (2020) (filled orange circles), two damped Lyman alpha (DLA) systems from De Cia et al. (2018, kindly provided by C. Péroux, priv. comm.) (open orange circles, one a lower limit due to its large impact parameter), and four gamma-ray burst (GRB) host galaxies with Z_g measurements from multiple metal absorption lines (Wiseman et al. 2017) (open orange stars). These systems all have robust measurements for their host stellar mass and uncertainties in their Z_g estimates of < 0.45 dex.

The modified model is in relatively good agreement with the ensemble of direct metallicity measurements compiled here, although the number of such observed systems is currently quite small. The modified model also agrees well with the observed evolution reported by Hunt et al. (2016). The PP04-N2 diagnostic used in that study agrees reasonably well with D16-NS2 at $z = 0$ for galaxies with $\log_{10}(M_*/M_\odot) \sim 10.0$, although less so at higher and lower masses.

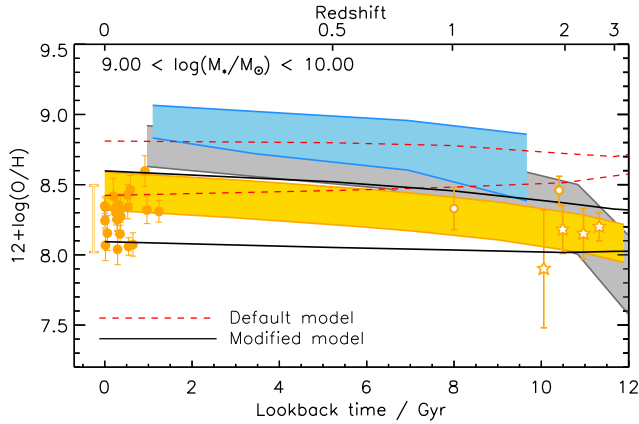


Figure 11. The evolution of ISM metallicity (Z_g) in star-forming galaxies as a function of lookback time, for galaxies in the mass range $9.0 \leq \log_{10}(M_*/M_\odot) < 10.0$. Black solid lines bracket the range of mean Z_g for this mass range from the modified L-GALAXIES 2020 model. Red dashed lines indicate the same for the default model. Shaded regions denote the evolution in Z_g inferred from the MZ_gR studies of Maiolino et al. (2008, grey), Zahid et al. (2014, blue), and Hunt et al. (2016, yellow). The orange/white bar (offset to slightly negative redshift for clarity) represents the range of Z_g found for galaxies in this mass range from our MaNGA sample. Filled orange circles represent individual systems with T_e -based Z_g estimates from Yates et al. (2020). Open orange circles represent DLA systems (quasar IDs: Q0302-223 and Q2206-199) with absorption-line-based Z_g from De Cia et al. (2018). Open orange stars represent GRB host galaxies (GRB050820A, GRB081008, GRB120119A, and GRB121024A) with absorption-line-based Z_g from (Wiseman et al. 2017) and stellar masses from Krühler et al. (2015); Perley et al. (2016).

The other two observational studies shown in Fig. 11 suggest much higher Z_g at low redshift, but similar Z_g at high redshift, and therefore a greater overall evolution over cosmic time. Interestingly, the majority of previous galaxy evolution models have compared and/or calibrated their MZ_gRs at $z = 0$ to SL diagnostic measurements similar to those used by Maiolino et al. (2008) and Zahid et al. (2014). This approach has led to the conclusion that the Z_g evolution of ~ 0.3 dex seen in models could be insufficient. However, an important result of the work presented here is that the rate of Z_g evolution seen in the majority of cosmological galaxy evolution models, including our modified model, is in fact in good agreement with the latest observational data. Most recently, Sanders et al. (2020) have measured the MZ_gR evolution from $z \sim 3.3$ to 0 using the MOSDEF survey, and have found an average increase in Z_g of 0.35 dex at $\log_{10}(M_*/M_\odot) = 10.0$, also in good agreement with our modified L-GALAXIES 2020 model.

The bottom panel of Fig. 10 shows the evolution of the MZ_gR from $z = 5$ to 0 for the modified model (with the mean mass-weighted Z_* from all radial rings considered here). Similarly to the MZ_gR, we see a consistent evolution at fixed mass over cosmic time. There is an increase in Z_* of $\Delta(Z_*) \sim 0.24$ dex from $z \sim 2$ to 0 in the modified model, which is in good agreement with the combined evolution observed by Ferreras et al. (2019) and Gallazzi et al. (2014), who found $\Delta(Z_*) \sim 0.07 \pm 0.07$ dex from $z \sim 2$ to 0.5 and $\Delta(Z_*) \sim 0.12 \pm 0.05$ dex from $z \sim 0.5$ to 0.1, respectively, for galaxies with $\log_{10}(M_*/M_\odot) \sim 11.0$.

We also find a much reduced evolution in the MZ_gR for ETGs compared to star-forming galaxies in L-GALAXIES 2020, in agreement with observations (e.g. Kriek et al. 2019; Estrada-Carpenter et al. 2019; Leethochawalit et al. 2019; Lonoce et al. 2020). At

$\log_{10}(M_*/M_\odot) = 11.0$, Z_* increases by only 0.04 dex from $z = 2$ to 0 for ETGs in the modified model. This is due to the relative lack of metal production in such quiescent systems at late times.

Regarding CGM metallicities at higher redshift, the general consensus from X-ray studies of the IGrM and ICM is that a significant fraction of the present-day iron abundance was already in place by $z \sim 1 - 2$ (e.g. Balestra et al. 2007; Anderson et al. 2009; McDonald et al. 2016). For example, McDonald et al. (2016) conclude that the metallicity (i.e. the metal to hydrogen ratio) in the ICM at $z = 1$ was already at least 60 per cent of that seen in clusters today. This scenario is in line with the early build-up of metals also seen in the stellar populations of ETGs discussed above.

In L-GALAXIES 2020, both the default and modified models broadly reproduce this observed trend for the ICM. In the default model, the mean ‘iron abundance fraction’ within r_{200} (i.e. $[\text{Fe}/\text{H}]_{200,z}/[\text{Fe}/\text{H}]_{200,z=0}$) for clusters with $\log(kT_{500,z=0}/\text{keV}) > 0.1$ is already 0.80 at $z = 1$ and increases to 0.88 by $z = 0.5$. This is similar to the result found by Yates et al. (2017), who studied an earlier version of L-GALAXIES which assumed f_{hot} values of 0.0.

The modified L-GALAXIES 2020 model shows an even smaller evolution at late times, with $[\text{Fe}/\text{H}]_{200,z}/[\text{Fe}/\text{H}]_{200,z=0} = 0.84$ at $z = 1$ and 0.89 at $z = 0.5$. This puts the modified model in somewhat better agreement with the observed rate of the ICM iron abundance evolution, notwithstanding the very large scatter in observed $[\text{Fe}/\text{H}]_{200}$ measurements (see Yates et al. 2017, section 6.5).

In conclusion, we find that the modified L-GALAXIES 2020 model is in better agreement with a range of higher-redshift global metallicity observations than earlier versions of the model. These improvements are primarily due to the implementation of increased direct enrichment of the CGM by SNe, which decreases the amount of metal mixing in the ISM and therefore lowers the gas and stellar metallicities inside galaxies, while increasing the metal content present in the hot gas surrounding galaxies, groups, and clusters.

4.3 Metallicity profiles at redshift zero

In the upper panels of Fig. 12, we show the stacked radial Z_g profiles out to $2.5 R_e$ for star-forming disc galaxies, split into four mass bins. For each mass bin, average profiles are obtained by taking the mean metallicity in annuli of $0.2 R/R_e$ width. Solid black lines and dashed red lines represent the mean profile from the modified and default L-GALAXIES 2020 models, respectively. Filled orange points represent the mean profile from our MaNGA sample, with Z_g calculated using the D16-N2S2 diagnostic and the vertical bars representing the 1σ spread in Z_g measurements in each radial bin.

There is promising agreement between the radial profiles in the modified model and the MaNGA observations. This is partly by construction, as we have used the *normalisation* of the observed low-redshift metallicity profiles as a guide when setting the values of the modified GCE parameters (see Section 2.1). This shows that there is a clear improvement in the match between observed profiles and L-GALAXIES 2020 when a significant amount of direct CGM enrichment is allowed.

In the highest-mass bin, the mean profile for the modified model is flatter than seen in our MaNGA sample. However, other observational data suggests that such flatter profiles are indeed present in massive disc galaxies. This is shown in the lower panels of Fig. 12, where Z_g profiles from the MUSE Atlas of Discs (MAD) sample are also shown (Erroz-Ferrer et al. 2019, open orange circles). That study utilised MUSE observations of 38 spiral galaxies at $z < 0.013$ which lie on the star-forming main sequence and have inclinations of $< 70^\circ$,

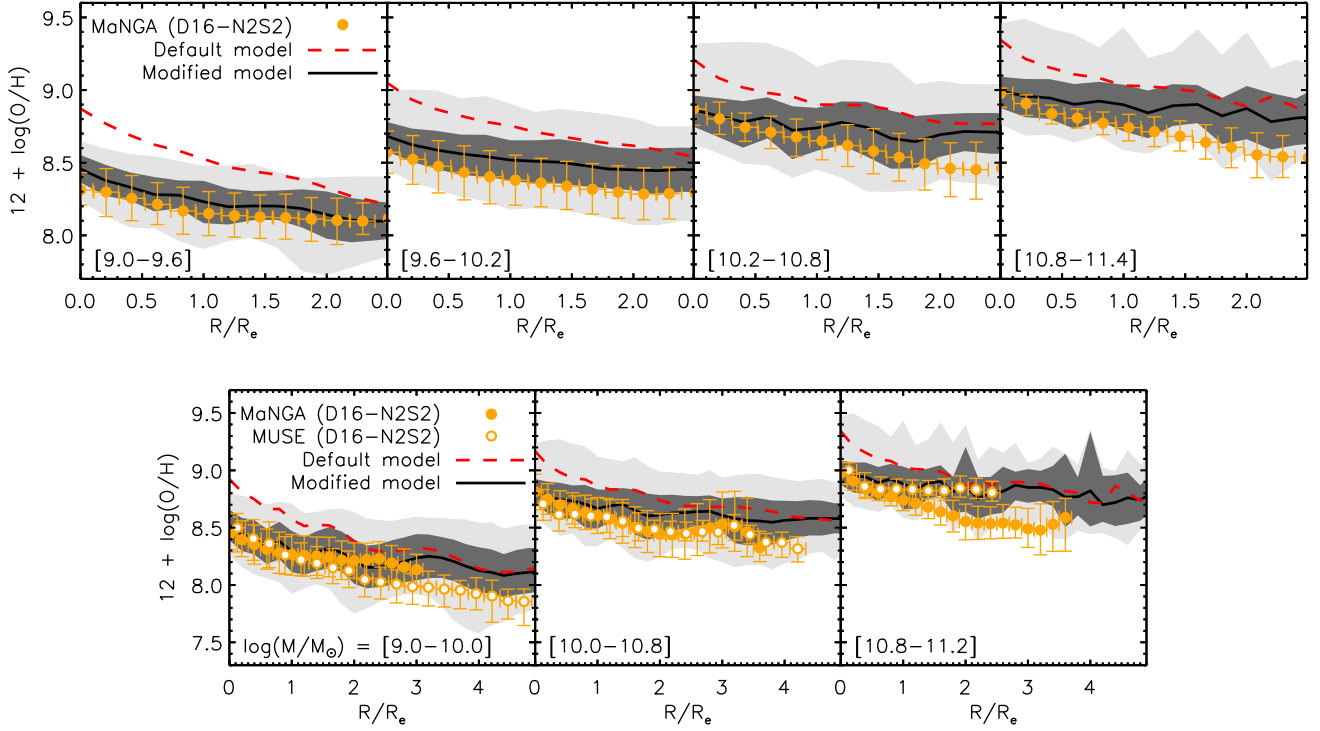


Figure 12. Top panels: Radial Z_g profiles out to $2.5R_e$ for galaxies in four mass bins. Black solid lines represent the modified model (with dark and light grey contours representing the 1σ and 2σ spread, respectively), red dashed lines represent the default model, and filled orange circles represent our MaNGA sample (with vertical bars representing the 1σ spread in Z_g). Bottom panels: The same as the top panels, but with profiles shown out to out to $5R_e$. Data is re-binned here into only three mass bins, in order to compare with the data from Erroz-Ferrer et al. (2019) for the MUSE/MAD sample (open orange circles).

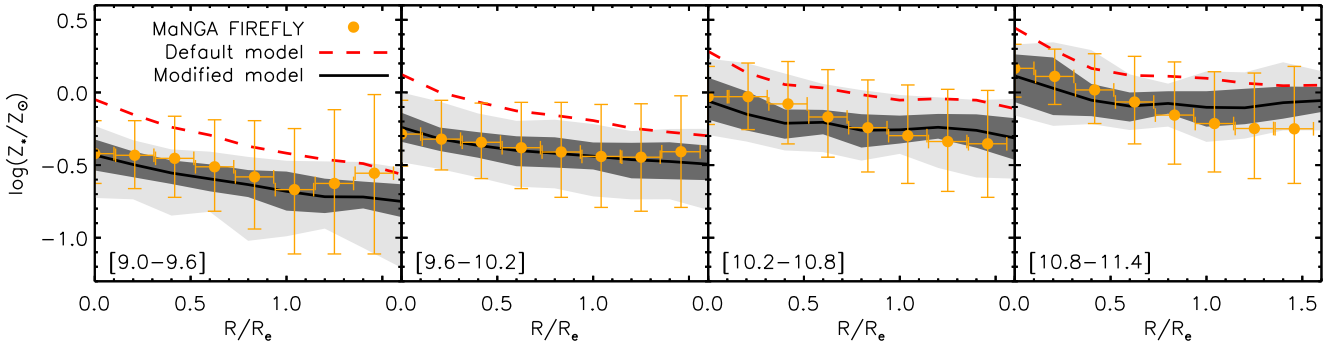


Figure 13. Radial Z_* profiles out to $1.6R_e$ for galaxies in four mass bins. Lines, contours, and colours are as in Fig. 12. Radial profiles for the MaNGA survey are constructed using the Z_* measurements made using FIREFLY (Goddard et al. 2017).

to measure Z_g profiles using the same D16-N2S2 diagnostic used here for our MaNGA sample. The MAD sample exhibits flatter radial profiles beyond $\sim 0.3R_e$ in massive galaxies, while corroborating the steeper profiles seen in our MaNGA sample at intermediate masses.

We note here that the MaNGA and MUSE IFUs have different spatial resolutions. The lower resolution of MaNGA (equating to $\sim 1-2$ kpc for our MaNGA sample, compared to an average of ~ 100 pc for the MAD sample) could become problematic when measuring Z_g at large galactocentric radii, as S/N tends to be lower and contamination from diffuse ionised gas (DIG) can become more significant (see also Poetrodjojo et al. 2019). However, lower resolution should artificially *flatten* radial profiles, rather than steepen them

(see e.g. Acharyya et al. 2020). In the case of the MUSE data, Erroz-Ferrer et al. (2019) were able to disentangle the contributions from HII regions and DIG in their sample, due to the higher resolution. Therefore, we tentatively conclude that the radial profiles provided by MUSE are more representative of the true distribution of metals in the ISM of massive disc galaxies, and find it promising that the modified L-GALAXIES 2020 model reproduces these profiles best.

Fig. 13 shows the radial profiles for stellar metallicity in disc galaxies, again split into four mass bins. We find good agreement between the modified L-GALAXIES 2020 model and the profiles from our MaNGA sample, particularly within $\sim 1R_e$, although we note the large spread in the observed Z_* at fixed radius. The modified

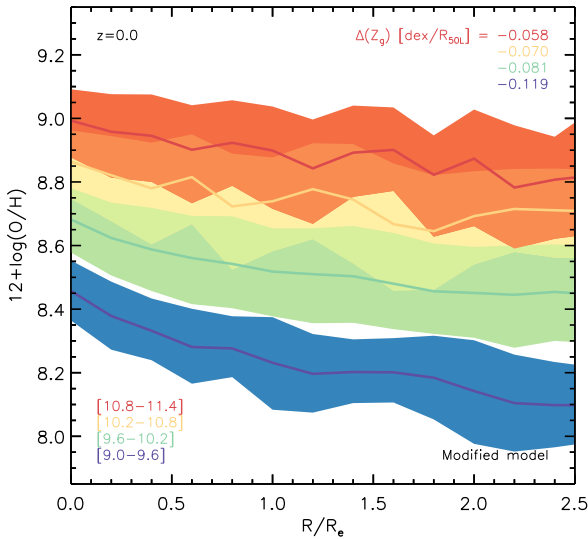


Figure 14. Mean radial Z_g profiles for star-forming, disc galaxies at $z = 0$ from our modified model, split into four mass bins. The 1σ spreads are illustrated by shaded regions. The mean slope in dex/ R_e from linear fits to the Z_g profile between 0.5 and $2R_e$ for each galaxy are reported for each mass bin in the top-right corner.

model (black solid line) is again a better fit to the data than the default model (red dashed line). However, as with the Z_g profiles, the modified model exhibits flatter Z_* profiles at large radii in massive galaxies than is seen in our MaNGA sample. It is again unlikely that lower spatial resolution is causing artificially steepened Z_* profiles in our MaNGA data. Therefore, this discrepancy between model and observations could instead indicate a shortcoming of our modified model in reproducing the metal content in discs at large radii (see Section 4.6.2).

We note here that the stellar bulge component is not included when plotting the radial Z_* profiles for our model galaxies in Fig. 13. This is because bulges are not yet resolved into self-consistent radial rings in L-GALAXIES 2020, so their spatial metallicity distribution is unknown. This issue is somewhat mitigated by the fact that we only consider model systems with relatively minor bulges, requiring a bulge-to-total mass ratio of < 0.3 (see Section 2.3). Likewise, we also expect the contribution from bulges in our comparison MaNGA sample to be minimal, as these systems have been specifically selected to have high sSFR, an inclination of $< 60^\circ$, and a clear spiral morphology from visual inspection (see Section 3.1).

4.4 Are metallicity profiles mass dependent?

There is currently no clear consensus in the observational literature as to whether Z_g profiles are dependent on stellar mass in nearby galaxies. Using a variety of different IFUs and Z_g diagnostics, some observational studies have suggested steeper slopes in more massive galaxies (e.g. Belfiore et al. 2017; Poetrodjojo et al. 2018), others flatter slopes in more massive galaxies (e.g. Kaplan et al. 2016; Erroz-Ferrer et al. 2019), and others no clear mass dependence at all (e.g. Sánchez et al. 2014; Lian et al. 2018b). This provides a good opportunity for galaxy evolution models such as L-GALAXIES 2020 to investigate metallicity profiles, as they work from a set of fundamental theoretical assumptions to provide a physical explanation for a given trend that is independent of observational biases.

Fig. 14 shows the binned Z_g profiles for $z = 0$ disc galaxies in the

modified L-GALAXIES 2020 model with all four mass bins plotted together. We have also calculated a linear fit to every model galaxy's Z_g profile between 0.5 and $2R_e$, and report the *mean* of the slopes in dex/ R_e for each mass bin in the top right corner. There is a clear, yet rather weak, dependence of the slope, $\Delta(Z_g)$, on stellar mass in the modified model, such that lower-mass galaxies have steeper $\Delta(Z_g)$. A similar mass dependence is also seen for the model Z_* slopes.

This trend is more clearly represented in Fig. 15, where $\Delta(Z_g)$ is shown as a function of stellar mass. Slopes are measured in dex/ R_e in the top panel, and dex/kpc in the bottom panel. Filled circles represent the *median* $\Delta(Z_g)$ in four mass bins from the modified model (black), default model (red), our MaNGA sample (filled orange), and the MAD sample (open orange). For the model and MaNGA samples, the median values have been calculated following the method of Belfiore et al. (2017), by azimuthally averaging the Z_g in radial bins for each galaxy, then taking its slope from an unweighted linear fit between 0.5 and $2R_e$ (considering only galaxies with ‘clean’ Z_g measurements in four or more radial bins in this range), and then taking the median of these slopes in each mass bin. For the MAD sample, we take the individual slope measurements provided by Erroz-Ferrer et al. 2019 in their table 1. In this case, only galaxies with Z_g measurements for HII regions in two or more 0.3 -dex-wide radial bins between 0.5 and $2R_e$ were considered.

When comparing the default and modified models to each other, we see that Z_g gradients are overall flatter (although still predominantly negative) in the modified model, especially at lower mass. This is caused by the enhanced direct CGM enrichment, as described in detail in the next section.

Regarding the observations, we find that the median $\Delta(Z_g)$ for low-mass galaxies in our MaNGA sample is particularly sensitive to (a) the SL Z_g diagnostic chosen, and (b) whether or not a spiral morphology is required. For example, when measured in dex/ R_e , the median slope for the lowest-mass bin flattens from -0.148 when using the D16-N2S2 diagnostic to -0.068 when using the M08-R23 diagnostic. Similarly, this median value decreases from -0.148 to -0.098 when not selecting on morphology. This latter change is likely due to a significant number of low-mass irregular galaxies entering the sample, which do not contain well-structured discs from which meaningful radial Z_g profiles can be obtained. We emphasise here that the clear majority of low-mass galaxies in MaNGA appear to be of non-spiral morphology. For example, the number of MaNGA galaxies in our lowest two mass bins increases by a factor of 5.0 and 2.7 , respectively, when allowing all morphologies into the sample. This increase is reduced to factors of 1.4 and 1.5 , respectively, for the highest two mass bins, reflecting the fact that massive star-forming galaxies more commonly have spiral morphologies. We also acknowledge that low-mass, disc-dominant galaxies which do not exhibit visible spiral structure may be excluded from our MaNGA sample.

The combination of using the M08-R23 Z_g diagnostic and relaxing the spiral morphology requirement decreases the median $\Delta(Z_g)$ for our lowest-mass bin to -0.058 dex/ R_e , with this value being just consistent with 0.0 within the 1σ spread. This could therefore partly explain the near-flat median profiles reported for low-mass galaxies by Belfiore et al. (2017) when using the M08-R23 or PP04-O3N2 diagnostics and not explicitly selecting for spiral or disc-dominant systems. However, biases to the D16-N2S2 diagnostic due to residual dependences on SFR could also play a role (see Section 3.2).

The presence of galactic bars could also contribute to a flattening of Z_g profiles in low-mass galaxies (Zurita et al. 2021b). Such dynamical components can funnel gas towards the centres of galaxies, redistributing their metals. This process can have a larger effect in

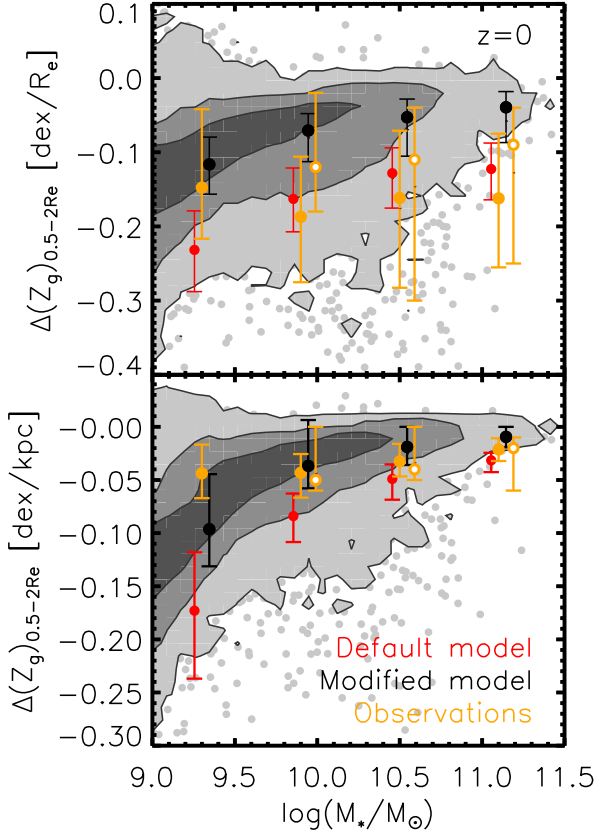


Figure 15. *Top panel:* Z_g profile slope, $\Delta(Z_g)$, in units of dex/R_e as a function of stellar mass for star-forming disc galaxies at $z = 0$. Grey contours and points represent the whole sample from the modified model. Red and black points represent the median $\Delta(Z_g)$ fit between 0.5 and $2R_e$ for the default and modified L-GALAXIES 2020 model, respectively. Filled orange circles represent the same median $\Delta(Z_g)$ from our MaNGA sample. Open orange circles represent the median $\Delta(Z_g)$ from the MUSE/MAD sample (Erroz-Ferrer et al. 2019). In all cases, vertical bars represent the 16th–84th percentile range in $\Delta(Z_g)$ for each mass bin. *Bottom panel:* Same as top panel, but with slopes measured in dex/kpc .

systems with large bar-to-total stellar mass ratios. However, it is more likely that the residual flattening seen in the lowest-mass MaNGA bin in Fig. 15 is due to spatial resolution. In their hydrodynamical simulations of disc galaxies, Acharyya et al. (2020) found that measured Z_g slopes can be artificially flattened by > 20 per cent for data with the spatial resolution and average PSF of MaNGA, with this effect being stronger for systems which have steeper ‘true’ profiles. This could play a role in explaining why our MaNGA profiles appear somewhat shallower than those of the MAD sample for the lowest-mass bin in Fig. 12.

The top panel of Fig. 15 indicates that Z_g profile slopes in the modified model are flatter than in the observations when measured in dex/R_e . However, we note that our MaNGA galaxies have systematically larger R_e than those in both the MUSE sample and L-GALAXIES 2020 at fixed stellar mass (noting that the model reproduces the typical R_e found in large populations of local, star-forming galaxies, see Henriques et al. 2020, section 4.2). The predominance of less compact stellar discs in our MaNGA sample is mainly due to the spiral morphology requirement, which preferentially removes low-mass, compact systems. Such an anti-correlation between disc size and $\Delta(Z_g)$ in MaNGA is also found by Boardman et al. (2021).

Therefore, we also compare the median $\Delta(Z_g)$ in units of dex/kpc in the bottom panel of Fig. 15. We find an improved agreement between the modified model, the MUSE sample, and the MaNGA sample in this case, suggesting that part of the discrepancy seen when using dex/R_e is indeed due to differences in R_e at fixed mass among the samples.

When considering trends with stellar mass, we find that above $\log_{10}(M_*/M_\odot) \sim 10.0$, all the observational and model samples studied here indicate a weak flattening of the slope with increasing stellar mass. The change in median $\Delta(Z_g)$ from $\log_{10}(M_*/M_\odot) \sim 9.9$ to 11.1 is quite similar between the modified model and observations, with $0.026 \text{ dex}/R_e/\log(M_*)$ for the modified model, compared to $0.025 \text{ dex}/R_e/\log(M_*)$ for the MAD sample and $0.021 \text{ dex}/R_e/\log(M_*)$ for our MaNGA sample. A similar agreement is seen when measuring slopes in dex/kpc .

Overall, our results are in best qualitative agreement with the findings from higher-resolution IFUs such as VIRUS-P and MUSE (e.g. Kaplan et al. 2016; Erroz-Ferrer et al. 2019), where a weak positive correlation between M_* and $\Delta(Z_g)$ is seen. Also, both Pilyugin et al. (2019) and Bresolin (2019) report a weak flattening of Z_g profiles with increasing stellar mass for a combination of long-slit, CALIFA, MaNGA, and MUSE spectra. Although, Bresolin 2019 only find this trend when slopes are measured in dex/kpc (see also Tissera et al. 2019). Similarly, Zurita et al. (2021a,b) find a positive correlation between $\Delta(Z_g)$ in dex/kpc and B-band luminosity for a large collection of HII regions from 20 unbarred galaxies with $i < 70^\circ$. Their result holds when measuring Z_g via either the T_e method or a range of SL Z_g diagnostics.

At lower masses, the good agreement found between our results and those of the above studies could also be due to the selection of spiral galaxies in all cases. Studies that find gradients flattening at low masses (e.g. Belfiore et al. 2017) tend to instead use the entire galaxy population without pre-selecting on morphology and, since most low-mass galaxies are irregular, their flat metallicity gradients dominate the statistics.

Given the weakness of the $M_* - \Delta(Z_g)$ correlation found in L-GALAXIES 2020, our results are also consistent with the largely mass-independent slopes reported by Sánchez et al. (2014) and Sánchez-Menguiano et al. (2016) using CALIFA, Lian et al. (2018b) using MaNGA, and Carton et al. (2018) using spatially-binned MUSE spectra of galaxies at $0.1 \lesssim z \lesssim 0.8$.

In the following section, we discuss the evolutionary processes taking place in L-GALAXIES 2020 that lead to the metallicity profiles present at redshift 0.

4.5 The evolution of metallicity profiles

In this section, we focus on results from L-GALAXIES 2020 run on the MILLENNIUM-II simulation, as this provides the higher resolution needed to study the low-mass progenitors of model galaxies back to high redshift.

When studying an earlier version of L-GALAXIES, Fu et al. (2013) established that the steepness of Z_g profiles depended on the merger history of the galaxy, as implied by its present-day bulge-to-total stellar mass ratio (B/T). When considering all model galaxies at $z = 0$, they found that those with larger B/T ratios had flatter Z_g profiles (when measured from the centre out to the far edge of the disc). In this present work, we instead focus only on disc-dominant ($B/T < 0.3$), star-forming galaxies in L-GALAXIES 2020, and measure profiles within $0.5 - 2 R_e$, in order to better compare to observations. For this sample, we do not find a strong correlation between B/T and

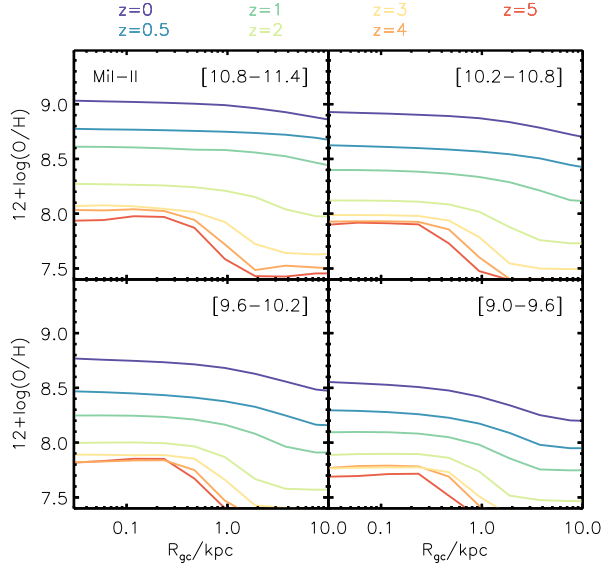


Figure 16. The evolution of radial Z_g profiles (as a function of galactocentric radius) for star-forming, disc galaxies selected at $z = 0$ in the modified model run on MILLENNIUM-II. Galaxies are split into four mass bins according to their stellar mass at $z = 0$.

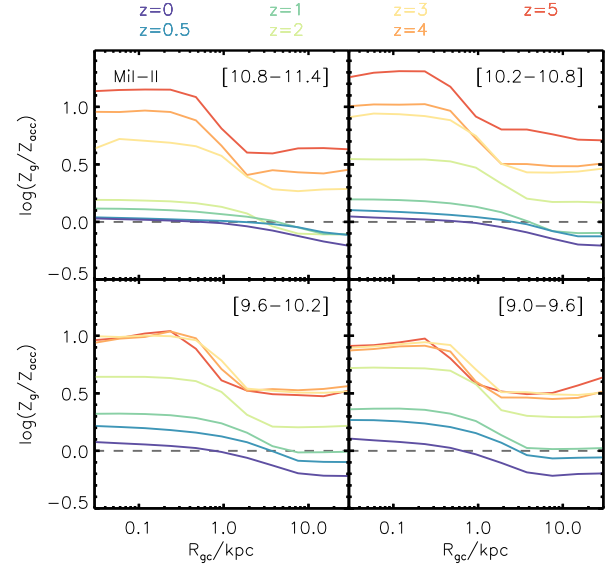


Figure 18. The evolution of the ratio of ISM oxygen abundance to accreted oxygen abundance (Z_g/Z_{acc}) for the same model galaxies as shown in Fig. 16. Dashed grey lines indicate an equal oxygen abundance in the ISM and accreted gas. Values of $\log(Z_g/Z_{acc})$ above 0 indicate dilution of the ISM, whereas values below 0 indicate enrichment of the ISM.

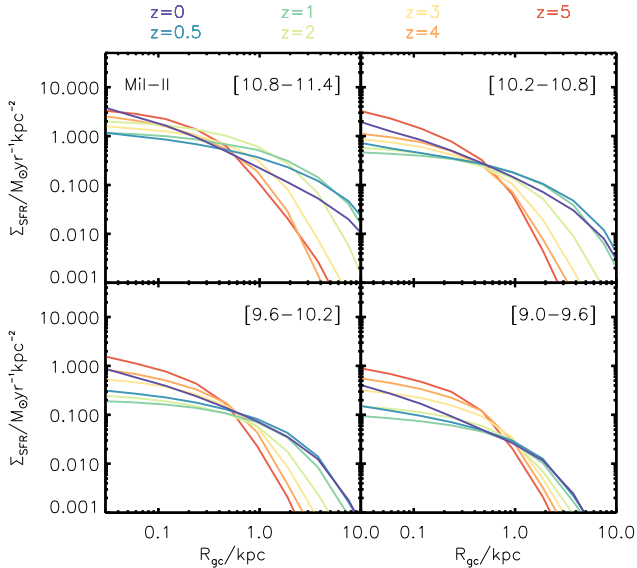


Figure 17. The evolution of radial Σ_{SFR} profiles for the same model galaxies as shown in Fig. 16.

$\Delta(Z_g)$, indicating that it is mainly secular processes that determine the differences in Z_g profiles seen in our model discs.

There are three main secular processes driving the evolution of metallicity profiles in L-GALAXIES 2020: *inside-out growth* (i.e. the spread of star formation out to larger radii over time), *radial gas inflows*, and *accretion of pre-enriched gas* from the CGM. The relative importance of these three processes determines the characteristic metallicity profiles seen at different masses and in different versions of the L-GALAXIES 2020 model.

Fig. 16 shows the evolution of mean Z_g profiles as a function of galactocentric radius (R_{gc}) in the modified model, from redshift 5

to 0. In each mass bin, star-forming disc galaxies are selected at $z = 0$, and then their main progenitors are traced back to higher redshifts in order to obtain the evolution of the *same* systems over cosmic time. The evolution in Z_g profiles seen in Fig. 16 can be best explained by considering the inner and outer disc separately. At low radii (below ~ 1 kpc), on-going star formation (fuelled by radial inflows and cooling from the CGM) drives the increase in Z_g seen over cosmic time. At large radii (above ~ 1 kpc), inside-out growth and pre-enriched accretion drive the increase in Z_g .

The effect of inside-out growth is best illustrated by Fig. 17, which shows the evolution of SFR surface density profiles in our model disc galaxies. The Σ_{SFR} increases beyond ~ 1 kpc over cosmic time due to the formation of new H_2 at progressively larger radii as gas discs grow in size. This inside-out growth is significantly stronger in massive galaxies (top-left panel of Fig. 17) than their lower-mass counterparts (bottom-right panel of Fig. 17).

The effect of metal-rich accretion is best illustrated by Fig. 18, which shows the ratio of the oxygen abundance in the ISM to that in the accreted gas, Z_g/Z_{acc} , as a function of radius. Due to the high direct CGM enrichment efficiency in the modified model (and the instantaneous mixing approximation assumed for the CGM in L-GALAXIES 2020), gas accreted from the CGM can reach a higher metallicity than that in the low-density outskirts of galaxy discs. This leads to an enrichment at large radii, similar to the ‘galactic fountain’ mechanism proposed by Fraternali et al. (2013). In massive galaxies, such metal-rich accretion begins to occur from $z \sim 2$ (top-left panel of Fig. 18) and does so efficiently due to shorter cooling timescales. In low-mass galaxies, it does not begin until after $z \sim 1$ (bottom-right panel of Fig. 18) and does so at a lower rate due to longer cooling timescales.

We can therefore see that more significant in-situ star formation beyond ~ 1 kpc, and more efficient metal-rich accretion at low redshift, drive a stronger increase in the outer Z_g over time in massive disc galaxies than in their low-mass counterparts. This leads to the flatter Z_g profiles seen in massive galaxies by redshift 0, and hence

the weakly mass-dependent Z_g slopes discussed in Section 4.4. A similar evolution is also seen for the outer discs of Milky-Way-type galaxies in the AURIGA simulation (Grand et al. 2019), and to a lesser extent in EAGLE (Collacchioni et al. 2020). Although, the latter study also reports steeper Z_g profile slopes with increasing accretion rate for the inner disc.

In contrast to the modified model, star formation is the dominant driver of metal enrichment at all radii in the default model. 70 per cent of the oxygen synthesised and released by SNe is initially deposited into the ISM in the default model, allowing a lot of metals to immediately mix with the nearby star-forming gas. The gas accreted from the CGM is therefore on average more metal-poor than the ISM at all radii and redshifts, causing a net *diluting* effect. This leads to relatively higher Z_g in the centres of galaxies and consequently steeper Z_g gradients by $z = 0$.

We note here that AGN feedback has a relatively minor impact on the metallicity profiles in disc-dominant systems in L-GALAXIES 2020. This is because it is most effective in galaxies with large super-massive black holes (SMBHs) and hot gas reservoirs, acting to reduce or prevent further gas accretion onto the disc (see section S1.14 of the Supplementary Material). For star-forming main-sequence galaxies, such as those in our sample here, SMBH masses and their accretion rates are relatively low, leading to a relatively mild suppression of their net cooling rates (which remain on average at $\sim 1\text{--}10\text{ M}_\odot/\text{yr}$ by $z = 0$, see also Yates & Kauffmann 2014). However, alternative forms of AGN feedback formalism, which allow significant amounts of gas to be ejected from star-forming galaxies via AGN-driven outflows, could affect the metallicities in the ISM and CGM, and therefore also the evolution of disc metallicity profiles.

There have also been a number of observational studies of metallicity profiles at higher redshift recently (e.g. Troncoso et al. 2014; Stott et al. 2014; Leethochawalit et al. 2016; Curti et al. 2020b; Wang et al. 2020; Gillman et al. 2021). In general, these studies suggest that (a) profiles are rather flat at all redshifts back to $z \sim 2.5$, albeit with a wide spread in $\Delta(Z_g)$ (see Hemler et al. 2020), and (b) strong, metal-rich galactic outflows are required in order to explain this. These findings are in reasonable qualitative agreement with the modified L-GALAXIES 2020 model, which allows highly efficient metal removal from galaxies via outflows. For example, when selecting galaxies *at fixed mass* (rather than as direct progenitors of present-day galaxies), and measuring $\Delta(Z_g)$ in dex/kpc across a radial range of $\sim 0\text{--}10\text{ kpc}$ (as is typically the case for higher-redshift observations), we find that for galaxies with $9.6 \leq \log_{10}(M_*/\text{M}_\odot) < 10.2$ that $\Delta(Z_g) \sim -0.08\text{ dex/kpc}$ on average at $z \sim 2$, flattening only mildly to -0.04 dex/kpc by $z = 0$.

However, the heterogeneity and limited resolution of the currently available observational data at high redshift make more detailed comparisons with models difficult. The measured Z_g slope in an observed high-redshift galaxy depends sensitively on a number of often uncontrollable or uncertain factors, such as its inclination, morphology, the radial range covered, radial resolution, normalisation chosen (e.g. R/R_e or R/kpc), and complex sample selection biases. Additionally, some SL Z_g diagnostics are expected to be less applicable to high-redshift galaxies than others, due to differences between the gas properties within these high-redshift systems and those at low redshift which are used for calibration (e.g. Cullen et al. 2014; Strom et al. 2018). We therefore choose not to force a more detailed comparison between Z_g profiles at high redshift in observations and models in this work. The arrival of instruments such as JWST/NIRSpec, VLT/ERIS, and VLT/MOONS will facilitate a much more precise, accurate, and comprehensive comparison between models and observations in future.

4.6 Alternative model variants

4.6.1 A gas-density-dependent CGM enrichment efficiency

One way to further refine the outflow prescription in L-GALAXIES 2020 is to tie the CGM enrichment efficiency to the density of the ISM gas through which outflows must pass. Such approaches have been trialled before in the L-GALAXIES and GALFORM semi-analytic models (Yates et al. 2013; Lagos et al. 2013). Here, we explore an extension to this formalism, by setting the amount of direct CGM enrichment from SNe to be inversely proportional to the log of the local ISM density in each radial ring. The effective CGM enrichment efficiency of both SNe-II and SNe-Ia is then given by,

$$f_{\text{SNe,hot}} = \min \left[1.0, \frac{1.5}{\log_{10}(\Sigma_{\text{ISM}}/\text{M}_\odot\text{pc}^{-2})} \right], \quad (5)$$

where the value of the normalisation constant, $10^{1.5} \approx 32\text{ M}_\odot\text{pc}^{-2}$, is chosen to reflect the typical gas density below which the H_2 fraction drops to zero according to the Krumholz et al. (2009) prescription used in L-GALAXIES 2020 (see Section 2). Above this density, $f_{\text{SNe,hot}}$ decreases, reaching ~ 50 per cent at ISM densities of $\sim 1000\text{ M}_\odot\text{pc}^{-2}$.

The mean Z_g profiles for this ‘ Σ_{ISM} -dependent model’ (green) are shown in Fig. 19. This version of L-GALAXIES 2020 performs similarly to the modified model presented earlier in this work, except that it returns steeper slopes in the centres of galaxies due to the higher-density ISM present in these regions.⁸ This brings the Σ_{ISM} -dependent model into worse agreement with observations in terms of Z_g profile normalisation, but somewhat better agreement in terms of the median slope (see Section 4.4).

The Σ_{ISM} -dependent model fails to adequately reproduce the evolution of global metallicity at fixed mass. As in the default model, a slightly *inverse* evolution occurs at low mass due to the over-enrichment of the ISM at very early times followed by metal-poor accretion and radial inflow thereafter. We therefore conclude that highly-efficient direct CGM enrichment is also favoured in the denser centres of galaxies. This result could be compatible with the findings of some high-resolution ISM simulations (e.g. Gatto et al. 2017), in which pre-SN stellar winds and radiation are able to efficiently clear dense ambient gas away from SN sites, allowing for efficient SN-driven galactic winds to be driven (see Section 5).

4.6.2 A reduced maximum SN-II progenitor mass

Another way to reduce the Z_g in the ISM of model galaxies is to decrease the overall amount of oxygen produced in the universe. This can be most directly done by lowering the upper mass limit for stars that can contribute to chemical enrichment. In L-GALAXIES 2020, massive stars are assumed to contribute via stellar winds and SNe-II up to a maximum birth mass of $M_{\text{GCE,max}} = 120\text{ M}_\odot$. This limit was chosen due to the fact that such massive stars are known to exist in the real Universe (see Côté et al. 2016, and references therein), and that they are required by some chemical evolution models to match the element ratios seen in stars and HII regions in the solar neighbourhood (e.g. Portinari et al. 1998; François et al. 2004; Carigi et al. 2020). However, other observational studies have suggested that the upper mass limit for SN-II progenitors should be considerably lower (e.g. Smartt 2015; Davies & Beasor 2018; Schady et al. 2019), and other chemical evolution models have been successful in reproducing Milky Way constraints without requiring enrichment from stars

⁸ In L-GALAXIES 2020, ISM densities exceeding $32\text{ M}_\odot\text{pc}^{-2}$ are typically found within $\sim 1.2\text{ R}_e$ for disc galaxies at $z = 0$.

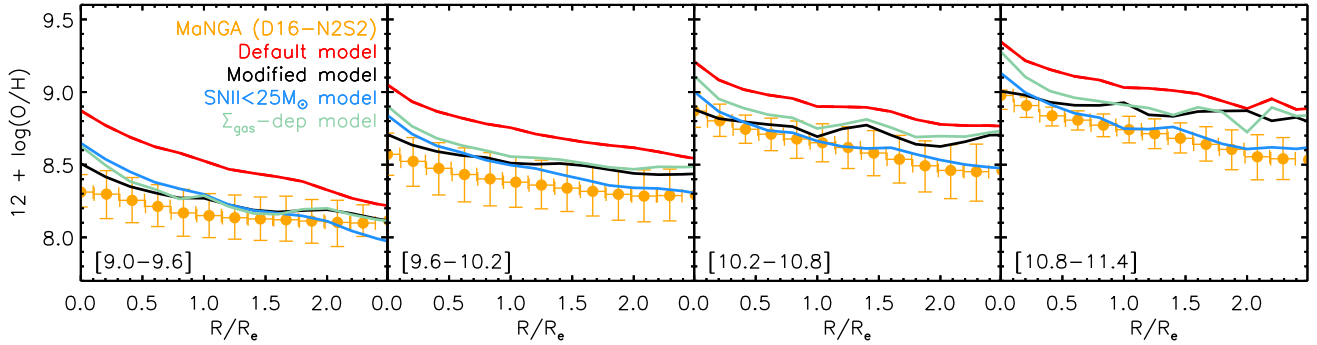


Figure 19. Mean radial Z_g profiles out to $2.5R_e$ for galaxies in four mass bins. The default (red), modified (black), Σ_{ISM} -dependent (green, see Section 4.6.1), and MAXGCEMass25 (blue, see Section 4.6.2) models are shown, along with our MaNGA sample (orange circles).

above $\sim 25 - 50 M_\odot$ (e.g. Kobayashi & Nakasato 2011; Côté et al. 2017).

Therefore, we assess the impact of lowering the mass limit of SN-II progenitors in L-GALAXIES 2020, by running a variant of the model with $M_{\text{GCE,max}} = 25 M_\odot$. This value was chosen to roughly mimic the findings of Ertl et al. (2016), which suggest that stars of mass $8 \leq \log_{10}(M_*/M_\odot) \leq 22$ are relatively efficient at forming SNe-II, whereas at higher masses there are only ‘islands of explosability’, with most stars directly collapsing into black holes. In this ‘MaxGCEMass25’ model, we maintain the upper mass threshold of the IMF at $120 M_\odot$, implying that stars between 25 and $120 M_\odot$ are formed but do not contribute at all to chemical enrichment or SN-driven winds. We also fix the values of all other L-GALAXIES 2020 parameters to those used in the default model, including the GCE parameters listed in Table 1.

Fig. 19 shows the radial Z_g profiles for this MaxGCEMass25 model as blue lines. We find a remarkable agreement in normalisation, slope, and scatter between the MaxGCEMass25 model and MaNGA data at high stellar mass. Although, we note that a shallower slope in high-mass galaxies is favoured by higher-resolution MUSE data (see Section 4.3). The Z_* profiles (not shown here) also reveal a good correspondence, with the MaxGCEMass25 model exhibiting slightly steeper slopes than the modified model out to large radii, in all mass bins. This is due to the lack of highly-enriched accretion onto the outskirts of galaxy discs in the MaxGCEMass25 model, as the f_{hot} parameter values are low.

A key difference between the MaxGCEMass25 and modified models should be the chemical abundances found *outside* galaxies, as these should differ greatly depending on whether massive stars are allowed to efficiently enrich the CGM or not at all. In Fig. 9, the TZ_{ICM} for the MaxGCEMass25 model (blue lines) is shown alongside those of the default and modified models. $[\text{Mg}/\text{H}]$ is clearly under-predicted by ~ 0.5 dex in the MaxGCEMass25 model relative to the other L-GALAXIES 2020 model variants and observations, even when considering the issues with Mg measurements discussed in Section 4.1.3. This under-abundance is caused by both the production and ejection of light α elements being greatly reduced in the MaxGCEMass25 model compared to the modified model. Heavier α elements, such as Si and S, are less affected by changes to $M_{\text{GCE,max}}$, because they are predominantly produced in lower-mass SN-II progenitor stars (see Portinari et al. 1998) which are allowed to enrich in all the versions of L-GALAXIES 2020 considered here.

Like the Σ_{ISM} -dependent model discussed above, the MaxGCEMass25 model also exhibits a lack of evolution in the MZ_g and

MZ_* over cosmic time, due to an over-retention of oxygen inside galaxies. This is in contradiction with the observations discussed in Section 4.2.

These shortcomings can be improved somewhat by increasing the value of $f_{\text{SNII,hot}}$ in the MaxGCEMass25 model, in line with what is already done in the modified model. However, we find that even when doubling the value of $f_{\text{SNII,hot}}$ to 0.6, the $[\text{Mg}/\text{H}]$ in the ICM is still too low by ~ 0.4 dex, and there is still effectively no evolution in Z_g over time at low mass. This suggests that there simply isn’t enough metal produced in the MaxGCEMass25 model considered here to adequately reproduce the chemical content observed in and around galaxies.

Allowing stars above $25 M_\odot$ to shed metal-rich winds *before* directly collapsing into black holes could help increase the overall metal budget in the MaxGCEMass25 model (see also Kobayashi et al. 2020; Gutcke et al. 2021). The combination of such pre-collapse wind enrichment with higher values of $f_{\text{SNII,hot}}$ will be an avenue of investigation with L-GALAXIES 2020 in future work.

5 COMPARISONS TO OTHER MODELS

5.1 Metal-rich winds

The main finding in this work, that a large fraction of the ejecta from SNe needs to be deposited directly into the CGM surrounding star-forming galaxies, is in good correspondence with earlier L-GALAXIES work by Fu et al. (2013) as well as a number of other theoretical studies. For example, Gibson et al. (2013) have found that metal-rich gas is efficiently removed from the centres of their two model L^* galaxies (the MaGICC simulations) when implementing an enhanced feedback prescription which enables 100 per cent of available SN energy to couple with the surrounding gas. This leads to flattened metallicity profiles at early times in these systems, similar to a sub-set of the high-redshift observations to which they compare. Metallicity profiles are similarly flattened in L-GALAXIES 2020 when switching from the default model to the modified model, with the latter being more efficient at removing metals from galaxies.

Similarly motivated by observed high-redshift Z_g slope estimates, Ma et al. (2017) show that the efficient SN feedback implemented into the FIRE simulations (Hopkins et al. 2014) causes flattened metallicity profiles. Of their five model galaxies with $\log_{10}(M_*/M_\odot) \geq 10.0$, four exhibit weakly-negative Z_g slopes across a similar radial range to that considered in this work, with $\Delta(Z_g) \lesssim -0.07$ dex/kpc. This

is in reasonable agreement with high-mass galaxies in L-GALAXIES 2020.

Despite the similarity between the results of these various models, there is an interesting difference in their feedback prescriptions. In MaGICC and FIRE, feedback is enhanced by allowing more material from the ISM to be entrained in galactic outflows, leading to increased CGM enrichment *and* increased mass-loading factors (see discussion by Mitchell et al. 2020). Conversely, in the modified L-GALAXIES 2020 model, enhanced CGM enrichment occurs *without* a corresponding increase in the mass-loading factor. This can be seen in Figs. 1 and 2, which show that the increased metal deposition into the CGM is accompanied by slightly lowered overall reheating rates and mass-loading factors, due to the reduced coupling between SNe ejecta and the ambient ISM. Physically speaking, this could be interpreted as low-density chimneys being opened-up in star-forming galaxies by on-going SN feedback.

Such a picture is seen in the high-resolution, stratified-disc simulations from the SILCC project (Walch et al. 2015), which have a spatial cell resolution of < 10 pc and initial gas surface density of $\Sigma_{\text{gas}} = 10 M_{\odot}/\text{pc}^2$. These simulations show that pre-SN stellar winds and ionising radiation can lower the density around the sites of SNe progenitors, allowing efficient galactic winds to be driven when the volume filling factor of hot gas in the ISM exceeds ~ 50 per cent (Gatto et al. 2017; Peters et al. 2017). Mass-loading factors typically reach 1-10 in SILCC (Girichidis et al. 2016; Gatto et al. 2017), in good agreement with those found in L-GALAXIES 2020 (see Fig. 2). In their simulations of similar size and spatial resolution to SILCC, Li et al. 2017 also find that 40-90 per cent of the metals ejected by SNe end up leaving the galaxy directly in such outflows.

These findings all point to a conclusion that *high-mass* galactic outflows are not necessarily required to reproduce the metallicities seen in main-sequence galaxies. Instead, more moderate mass-loading factors, accompanied by efficient *direct* CGM enrichment by SNe, can provide an equally viable solution.

5.2 MZR evolution

Collacchioni et al. (2018) have found that an explicit redshift dependence in the reheating rate is required to drive an evolution in Z_g at fixed mass in the SAG semi-analytic model. This modification boosts SN feedback in order to increase the amount of ISM gas reheated at high redshift. The original, unmodified prescriptions for calculating reheating and ejection energies in SAG are similar to those used in L-GALAXIES. Both formalisms rely on a dependence on the DM subhalo velocity, which naturally provides an evolution with both mass and redshift (see Fig. 1). Nonetheless, this alone is not enough to drive an evolution in the MZ_gR in our default model, in agreement with the findings of Collacchioni et al. (2018). However, such a reheating formalism *is* sufficient when coupled with a high, fixed direct CGM enrichment efficiency in our modified model. Our approach also has only a minimal effect on the cosmic SFRD evolution, in contrast to the modified SAG set-up (see their fig. 6).

Similarly to SAG, Lian et al. (2018a,c) are only able to simultaneously reproduce an evolution in the MZ_gR and MZ_* R for their stand-alone GCE model when implementing a strongly time- and mass-dependent f_{hot} parameter. We note that part of the motivation for such an approach is the large difference between the ISM and stellar metallicities inferred by Lian et al. (2018a) from their chosen low-redshift observations. This difference, reaching ~ 0.8 dex at low mass, requires particularly strong direct metal ejection at early times, with a value of $f_{\text{hot}} = 1.0$ being maintained over the first 9 Gyr for galaxies with $\log_{10}(M_*/M_{\odot}) = 9.0$. Due to the smaller difference

between Z_g and Z_* of ~ 0.2 dex we find for our MaNGA sample when using the D16-N2S2 diagnostic to calculate Z_g , as well as the additional astrophysics modelled in L-GALAXIES 2020, we find that such explicit time and mass dependencies of f_{hot} are not required in our models.

A mass (although not time) dependent $f_{\text{SNII,hot}}$ parameter was found by Somerville et al. (2015) to drive an MZ_gR evolution in the SANTA CRUZ semi-analytic model, when studying various combinations of H_2 formation, star formation, and metal outflow recipes. A model variant in which $f_{\text{SNII,hot}} \propto \exp(-M_{\text{vir}})$ was found to reduce star formation at early times, and therefore drive a greater evolution in Z_g below $z \sim 4$. Many of the other combinations considered returned a negligible or even inverted evolution in Z_g with cosmic time, as is also seen for our default model.

Finally, an evolution in the MZ_gR is seen in the ILLUSTRIS-TNG100 hydrodynamical model despite having an *increase* in the metal reheating efficiency over cosmic time, especially in higher-mass galaxies (Torrey et al. 2019). That study determined that Z_g evolution is primarily driven by changes in the ISM gas fraction, rather than the efficiency of metal removal via SN feedback.

The range of different approaches taken by the above models to reproduce the MZ_gR suggests that additional constraints, such as the evolution of metallicity profiles, are also important when trying to pin-down the key physical processes actually driving galactic chemical evolution.

5.3 Metallicity profiles

Recently, Tissera et al. (2019) found relatively flat slopes at $z = 0$ for their 592 model galaxies from the EAGLE hydrodynamical simulation. They report a weak correlation between $\Delta(Z_g)$ and stellar mass for secularly-evolving galaxies when measuring $\Delta(Z_g)$ in dex/kpc, and identify inside-out growth as one of the mechanisms driving flatter Z_g profiles in massive galaxies. Overall, these EAGLE results are in qualitative agreement with the findings from L-GALAXIES 2020 presented here, reflecting the similar chemical enrichment schemes implemented into the two models.

When extending their GCE model to account for metallicity gradients, Lian et al. (2018b, 2019) found that an additional radial dependence on the f_{hot} parameter enabled a better match to the slopes and normalisations of their preferred observed Z_g and Z_* profiles at $z = 0$. The main differences between the MaNGA data set used by Lian et al. (2018b, 2019) and that considered here are (a) the choice of SL Z_g diagnostic, (b) the use of VOR10 versus HYB10 datacubes for the gas-phase analysis, and (c) our spiral morphology requirement. When comparing to our preferred observational sample, the modified L-GALAXIES 2020 model does not require an additional radial dependence on f_{hot} .

Finally, Hemler et al. (2020) have recently investigated the evolution of Z_g profiles in the ILLUSTRIS-TNG50 simulation. At low redshift, there is good qualitative agreement between their findings and those of the modified L-GALAXIES 2020 model. For example, Hemler et al. (2020) find a weak correlation between stellar mass and $\Delta(Z_g)$ (when measured in dex/kpc) at $z = 0$. However, they report a consistent flattening of average Z_g profiles over cosmic time *at fixed mass* in ILLUSTRIS-TNG50. In contrast, Z_g profile slopes remain fairly constant over cosmic time at fixed mass in L-GALAXIES 2020, as discussed in Section 4.5. For example, the median $\Delta(Z_g)$ changes from -0.042 dex/kpc at $z = 2$ to -0.037 dex/kpc at $z = 0$ for the mass bin $9.6 \leq \log_{10}(M_*/M_{\odot}) < 10.2$ in our modified model, when measured between 0.5 and $2R_e$. This puts L-GALAXIES 2020 in better agreement with models such as MaGICC and FIRE. When in-

stead tracing the change in $\Delta(Z_g)$ for the same galaxies as they evolve over cosmic time, we do find a consistent flattening in L-GALAXIES 2020, as shown in Fig. 16. This highlights the importance of distinguishing between fixed-mass populations and individual galaxies when assessing and comparing the evolution of Z_g profiles.

6 CONCLUSIONS

In this work, we present a modified version of the L-GALAXIES 2020 galaxy evolution model. This modified model performs better than our default model in reproducing the gas and stellar radial metallicity profiles observed in low-redshift star-forming disc galaxies, as well as the present-day galaxy mass – metallicity relations for gas and stars, and their evolution back to $z \sim 2 - 3$. These improvements are achieved without significantly altering the good correspondence that L-GALAXIES 2020 has with other key galaxy population properties such as the stellar mass function, H I mass function, $M_* - \text{sSFR}$ relation, and cosmic SFR density evolution. In order to compare with IFU observations at low redshift, we have formed and derived radial profiles for a sample of 571 MaNGA star-forming disc galaxies, and also utilised MUSE galaxy profiles made available in the literature. The following key results are obtained:

- Highly-efficient direct enrichment of the CGM by SNe-II is required in L-GALAXIES 2020 to reproduce Z_g and Z_* profiles in nearby disc galaxies. ~ 90 per cent of SN-II ejecta directly enriching the CGM is preferred, with ~ 80 per cent for SNe-Ia (see Section 4.3). We find that values below ~ 75 per cent lead to an overly-enriched ISM and stellar disc in galaxies at both high and low redshift.
- Such high CGM enrichment efficiencies also enable L-GALAXIES 2020 to reproduce the stellar and gas-phase mass – metallicity relations at $z = 0$ and their evolution back to $z \sim 2 - 3$, as well as the metal content found in the hot gas surrounding star-forming galaxies, groups, and clusters (see Sections 4.1 & 4.2).
- We find a weak correlation between stellar mass and Z_g profile slope in the modified model at $z = 0$, such that more massive galaxies tend to have flatter profiles. This is in general agreement with both our MaNGA sample above $\log_{10}(M_*/M_\odot) \sim 10$ and other recent IFU studies (see Section 4.4).
- We note that this trend between stellar mass and Z_g profile slope in observational samples is sensitive to both the metallicity diagnostic and galaxy morphology cut chosen, particularly for low-mass systems (see Section 4.4). Slope measurements are also sensitive to the particular radial range and radial scaling chosen.
- The weakly mass-dependent Z_g slopes seen in L-GALAXIES 2020 are primarily caused by more efficient metal enrichment at large radii in massive galaxies than in low-mass galaxies. This enrichment is driven by a combination of inside-out growth and metal-rich accretion (see Section 4.5).
- We find that gas-density-dependent direct CGM enrichment efficiencies are also compatible with observed Z_g and Z_* profiles. However, values above ~ 60 per cent are still required in L-GALAXIES 2020, even for high-density regions near the centres of galaxies (see Section 4.6.1).
- Reducing the upper mass limit for SN-II progenitor stars to $25 M_\odot$ also reproduces the Z_g and Z_* profiles seen in low-redshift star-forming galaxies, without requiring strong direct CGM enrichment. However, this model variant severely under-predicts the magnesium abundances found in the intragroup and intracluster medium, as well as the observed evolution of the MZ_gR (see Section 4.6.2).

In future work, we intend to study the effects of combining high

efficiencies of metal ejection into the CGM with a reduced maximum SN-II progenitor mass in L-GALAXIES 2020, in tandem with a re-evaluation of the input stellar yield tables used. This will allow us to further constrain the chemical properties of both star-forming and quiescent galaxies at high redshift.

DATA AVAILABILITY

The L-GALAXIES 2020 source code, as well as example output catalogues from the default and modified models, are publically available at lgalaxiespublicrelease.github.io/. Complete output catalogues for the L-GALAXIES 2020 default model are also available on the MILLENNium database at gavo.mpa-garching.mpg.de/Millennium/. Additional L-GALAXIES data and the MaNGA derived data products presented here can be obtained from the main author upon request.

ACKNOWLEDGEMENTS

The authors would like to thank the referee for very helpful and constructive comments and suggestions, as well as Michael Blanton, Payel Das, Thales Gutcke, François Mernier, Céline Péroux, Doris Stoppacher, David Wake, Jessica Werk, Jabran Zahid, and Almudena Zurita, for valuable discussions during the undertaking of this work. BMBH acknowledges support from a Zwicky Prize fellowship. JF acknowledges the support by the Youth innovation Promotion Association CAS and Shanghai Committee of Science and Technology grant No.19ZR1466700. Part of this research was carried out on the HPC resources at the MPCDF in Garching operated by the Max Planck Society (MPG).

REFERENCES

- Acharyya A., Krumholz M. R., Federrath C., Kewley L. J., Goldbaum N. J., Sharp R., 2020, *MNRAS*, **495**, 3819
- Anderson M. E., Bregman J. N., Butler S. C., Mullis C. R., 2009, *ApJ*, **698**, 317
- Andrews B. H., Martini P., 2013, *ApJ*, **765**, 140
- Angulo R. E., Hilbert S., 2015, *MNRAS*, **448**, 364
- Angulo R. E., White S. D. M., 2010, *MNRAS*, **405**, 143
- Asplund M., Grevesse N., Sauval A. J., Scott P., 2009, *ARA&A*, **47**, 481
- Baldry I. K., Glazebrook K., Driver S. P., 2008, *MNRAS*, **388**, 945
- Baldry I. K., et al., 2012, *MNRAS*, **421**, 621
- Baldwin J. A., Phillips M. M., Terlevich R., 1981, *PASP*, **93**, 5
- Balestra I., Tozzi P., Ettori S., Rosati P., Borgani S., Mainieri V., Norman C., Viola M., 2007, *A&A*, **462**, 429
- Belfiore F., et al., 2017, *MNRAS*, **469**, 151
- Belfiore F., et al., 2019, *AJ*, **158**, 160
- Blanton M. R., Kazin E., Muna D., Weaver B. A., Price-Whelan A., 2011, *AJ*, **142**, 31
- Boardman N., et al., 2020, *MNRAS*, **491**, 3672
- Boardman N. F., Zasowski G., Newman J. A., Sanchez S. F., Schaefer A., Lian J., Bizyaev D., Drory N., 2021, *MNRAS*, **501**, 948
- Bouché N., et al., 2010, *ApJ*, **718**, 1001
- Boylan-Kolchin M., Springel V., White S. D. M., Jenkins A., Lemson G., 2009, *MNRAS*, **398**, 1150
- Bresolin F., 2008, in Israelian G., Meynet G., eds, *The Metal-Rich Universe*. p. 155 ([arXiv:astro-ph/0608410](https://arxiv.org/abs/astro-ph/0608410))
- Bresolin F., 2019, *MNRAS*, **488**, 3826
- Bresolin F., Gieren W., Kudritzki R.-P., Pietrzyński G., Urbaneja M. A., Carraro G., 2009, *ApJ*, **700**, 309
- Brinchmann J., Charlot S., White S. D. M., Tremonti C., Kauffmann G., Heckman T., Brinkmann J., 2004, *MNRAS*, **351**, 1151

- Bundy K., et al., 2015, *ApJ*, **798**, 7
- Calzetti D., Armus L., Bohlin R. C., Kinney A. L., Koornneef J., Storchi-Bergmann T., 2000, *ApJ*, **533**, 682
- Cappellari M., Copin Y., 2003, *MNRAS*, **342**, 345
- Carigi L., Peimbert A., Peimbert M., Delgado-Inglada G., 2020, *Rev. Mex. Astron. Astrofis.*, **56**, 235
- Carton D., et al., 2018, *MNRAS*, **478**, 4293
- Chabrier G., 2003, *PASP*, **115**, 763
- Collacchioni F., Cora S. A., Lagos C. D. P., Vega-Martínez C. A., 2018, *MNRAS*, **481**, 954
- Collacchioni F., Lagos C. D. P., Mitchell P. D., Schaye J., Wisnioski E., Cora S. A., Correa C. A., 2020, *MNRAS*, **495**, 2827
- Côté B., Ritter C., O'Shea B. W., Herwig F., Pignatari M., Jones S., Fryer C. L., 2016, *ApJ*, **824**, 82
- Côté B., O'Shea B. W., Ritter C., Herwig F., Venn K. A., 2017, *ApJ*, **835**, 128
- Cullen F., Cirasuolo M., McLure R. J., Dunlop J. S., Bowler R. A. A., 2014, *MNRAS*, **440**, 2300
- Curti M., Mannucci F., Cresci G., Maiolino R., 2020a, *MNRAS*, **491**, 944
- Curti M., et al., 2020b, *MNRAS*, **492**, 821
- D'Souza R., Vegetti S., Kauffmann G., 2015, *MNRAS*, **454**, 4027
- Davé R., Finlator K., Oppenheimer B. D., 2012, *MNRAS*, **421**, 98
- Davé R., Rafieferantsoa M. H., Thompson R. J., Hopkins P. F., 2017, *MNRAS*, **467**, 115
- Davé R., Anglés-Alcázar D., Narayanan D., Li Q., Rafieferantsoa M. H., Appleby S., 2019, *MNRAS*, **486**, 2827
- Davies B., Beasor E. R., 2018, *MNRAS*, **474**, 2116
- De Cia A., Ledoux C., Petitjean P., Savaglio S., 2018, *A&A*, **611**, A76
- De Lucia G., Blaizot J., 2007, *MNRAS*, **375**, 2
- De Rossi M. E., Bower R. G., Font A. S., Schaye J., Theuns T., 2017, *MNRAS*, **472**, 3354
- Dopita M. A., Kewley L. J., Sutherland R. S., Nicholls D. C., 2016, *Ap&SS*, **361**, 61
- Driver S. P., et al., 2018, *MNRAS*, **475**, 2891
- Elbaz D., et al., 2007, *A&A*, **468**, 33
- Emerick A., Bryan G. L., Mac Low M.-M., Côté B., Johnston K. V., O'Shea B. W., 2018, *ApJ*, **869**, 94
- Emerick A., Bryan G. L., Mac Low M.-M., 2020, *ApJ*, **890**, 155
- Erroz-Ferrer S., et al., 2019, *MNRAS*, **484**, 5009
- Ertl T., Janka H. T., Woosley S. E., Sukhbold T., Ugliano M., 2016, *ApJ*, **818**, 124
- Esteban C., Bresolin F., Peimbert M., García-Rojas J., Peimbert A., Mesa-Delgado A., 2009, *ApJ*, **700**, 654
- Esteban C., García-Rojas J., Carigi L., Peimbert M., Bresolin F., López-Sánchez A. R., Mesa-Delgado A., 2014, *MNRAS*, **443**, 624
- Estrada-Carpenter V., et al., 2019, *ApJ*, **870**, 133
- Ferland G. J., et al., 2013, *Rev. Mex. Astron. Astrofis.*, **49**, 137
- Ferreras I., et al., 2019, *MNRAS*, **486**, 1358
- François P., Matteucci F., Cayrel R., Spite M., Spite F., Chiappini C., 2004, *A&A*, **421**, 613
- Fraternali F., Marasco A., Marinacci F., Binney J., 2013, *ApJ*, **764**, L21
- Fu J., Guo Q., Kauffmann G., Krumholz M. R., 2010, *MNRAS*, **409**, 515
- Fu J., Kauffmann G., Li C., Guo Q., 2012, *MNRAS*, **424**, 2701
- Fu J., et al., 2013, *MNRAS*, **434**, 1531
- Gallazzi A., Bell E. F., Zibetti S., Brinchmann J., Kelson D. D., 2014, *ApJ*, **788**, 72
- Gatto A., et al., 2017, *MNRAS*, **466**, 1903
- Gibson B. K., Pilkington K., Brook C. B., Stinson G. S., Bailin J., 2013, *A&A*, **554**, A47
- Gillman S., et al., 2021, *MNRAS*, **500**, 4229
- Giovanelli R., Haynes M. P., Salzer J. J., Wegner G., da Costa L. N., Freudling W., 1994, *AJ*, **107**, 2036
- Girichidis P., et al., 2016, *MNRAS*, **456**, 3432
- Goddard D., et al., 2017, *MNRAS*, **466**, 4731
- Grand R. J. J., et al., 2019, *MNRAS*, **490**, 4786
- Guo Q., et al., 2011, *MNRAS*, **413**, 101
- Guo Q., et al., 2016, *MNRAS*, **461**, 3457
- Gutcke T. A., Pakmor R., Naab T., Springel V., 2021, *MNRAS*, **500**, 1–22 (2021)
- Haardt F., Madau P., 2012, *ApJ*, **746**, 125
- Haynes M. P., et al., 2011, *AJ*, **142**, 170
- Hemler Z. S., et al., 2020, arXiv e-prints, p. arXiv:2007.10993
- Henriques B. M. B., Thomas P. A., Oliver S., Roseboom I., 2009, *MNRAS*, **396**, 535
- Henriques B. M. B., White S. D. M., Thomas P. A., Angulo R., Guo Q., Lemson G., Springel V., Overzier R., 2015, *MNRAS*, **451**, 2663
- Henriques B. M. B., Yates R. M., Fu J., Guo Q., Kauffmann G., Srisawat C., Thomas P. A., White S. D. M., 2020, *MNRAS*, **491**, 5795
- Hirschmann M., De Lucia G., Fontanot F., 2016, *MNRAS*, **461**, 1760
- Hopkins P. F., Kereš D., Oñorbe J., Faucher-Giguère C.-A., Quataert E., Murray N., Bullock J. S., 2014, *MNRAS*, **445**, 581
- Hunt L., Dayal P., Magrini L., Ferrara A., 2016, *MNRAS*, **463**, 2002
- Jones M. G., Haynes M. P., Giovanelli R., Moorman C., 2018, *MNRAS*, **477**, 2
- Kaplan K. F., et al., 2016, *MNRAS*, **462**, 1642
- Kauffmann G., et al., 2003, *MNRAS*, **341**, 33
- Kewley L. J., Dopita M. A., 2002, *ApJS*, **142**, 35
- Kewley L. J., Ellison S. L., 2008, *ApJ*, **681**, 1183
- Knebe A., et al., 2018, *MNRAS*, **474**, 5206
- Kobayashi C., Nakasato N., 2011, *ApJ*, **729**, 16
- Kobayashi C., Karakas A. I., Lugaro M., 2020, *ApJ*, **900**, 179
- Kobulnicky H. A., Kewley L. J., 2004, *ApJ*, **617**, 240
- Kreckel K., Blanc G. A., Schinnerer E., Groves B., Adamo A., Hughes A., Meidt S., 2016, *ApJ*, **827**, 103
- Kreckel K., et al., 2020, *MNRAS*, **499**, 193
- Kriek M., et al., 2019, *ApJ*, **880**, L31
- Krühler T., et al., 2015, *A&A*, **581**, A125
- Krumholz M. R., McKee C. F., Tumlinson J., 2009, *ApJ*, **693**, 216
- Kudritzki R. P., Castro N., Urbaneja M. A., Ho I.-T., Bresolin F., Gieren W., Pietrzyński G., Przybilla N., 2016, *ApJ*, **829**, 70
- Lacerda E. A. D., et al., 2018, *MNRAS*, **474**, 3727
- Lagos C. d. P., Lacey C. G., Baugh C. M., 2013, *MNRAS*, **436**, 1787
- Leethochawalit N., Jones T. A., Ellis R. S., Stark D. P., Richard J., Zitrin A., Auger M., 2016, *ApJ*, **820**, 84
- Leethochawalit N., Kirby E. N., Ellis R. S., Moran S. M., Treu T., 2019, *ApJ*, **885**, 100
- Levesque E. M., Richardson M. L. A., 2014, *ApJ*, **780**, 100
- Li C., White S. D. M., 2009, *MNRAS*, **398**, 2177
- Li Y., Bresolin F., Kennicutt Robert C. J., 2013, *ApJ*, **766**, 17
- Li M., Bryan G. L., Ostriker J. P., 2017, *ApJ*, **841**, 101
- Lian J., Thomas D., Maraston C., Goddard D., Comparat J., Gonzalez-Perez V., Ventura P., 2018a, *MNRAS*, **474**, 1143
- Lian J., et al., 2018b, *MNRAS*, **476**, 3883
- Lian J., Thomas D., Maraston C., 2018c, *MNRAS*, **481**, 4000
- Lian J., Thomas D., Li C., Zheng Z., Maraston C., Bizyaev D., Lane R. R., Yan R., 2019, *MNRAS*, **489**, 1436
- Lilly S. J., Carollo C. M., Pipino A., Renzini A., Peng Y., 2013, *ApJ*, **772**, 119
- Lintott C. J., et al., 2008, *MNRAS*, **389**, 1179
- Lintott C., et al., 2011, *MNRAS*, **410**, 166
- Lonoce I., Maraston C., Thomas D., Longhetti M., Parikh T., Guarnieri P., Comparat J., 2020, *MNRAS*, **492**, 326
- Ma X., Hopkins P. F., Faucher-Giguère C.-A., Zolman N., Muratov A. L., Kereš D., Quataert E., 2016, *MNRAS*, **456**, 2140
- Ma X., Hopkins P. F., Feldmann R., Torrey P., Faucher-Giguère C.-A., Kereš D., 2017, *MNRAS*, **466**, 4780
- Madau P., Dickinson M., 2014, *ARA&A*, **52**, 415
- Maiolino R., Mannucci F., 2019, *A&ARv*, **27**, 3
- Maiolino R., et al., 2008, *A&A*, **488**, 463
- Mannucci F., Cresci G., Maiolino R., Marconi A., Gnerucci A., 2010, *MNRAS*, **408**, 2115
- Maoz D., Mannucci F., Brandt T. D., 2012, *MNRAS*, **426**, 3282
- Maoz D., Mannucci F., Nelemans G., 2014, *ARA&A*, **52**, 107
- Maraston C., 2005, *MNRAS*, **362**, 799
- Maraston C., Strömbäck G., 2011, *MNRAS*, **418**, 2785
- Marigo P., 2001, *A&A*, **370**, 194
- Martin C. L., Kobulnicky H. A., Heckman T. M., 2002, *ApJ*, **574**, 663

- McDonald M., et al., 2016, *ApJ*, **826**, 124
- McKee C. F., Krumholz M. R., 2010, *ApJ*, **709**, 308
- Mernier F., et al., 2018a, *MNRAS*, **478**, L116
- Mernier F., et al., 2018b, *MNRAS*, **480**, L95
- Mingozi M., et al., 2020, *A&A*, **636**, A42
- Mitchell P. D., Schaye J., Bower R. G., Crain R. A., 2020, *MNRAS*, **494**, 3971
- Okamoto T., Nagashima M., Lacey C. G., Frenk C. S., 2017, *MNRAS*, **464**, 4866
- Perley D. A., et al., 2016, *ApJ*, **830**, 13
- Peters T., et al., 2017, *MNRAS*, **466**, 3293
- Pettini M., Pagel B. E. J., 2004, *MNRAS*, **348**, L59
- Pilyugin L. S., Vílchez J. M., Thuan T. X., 2010, *ApJ*, **720**, 1738
- Pilyugin L. S., Grebel E. K., Zinchenko I. A., Nefedev Y. A., Vílchez J. M., 2019, *A&A*, **623**, A122
- Poetrodjojo H., et al., 2018, *MNRAS*, **479**, 5235
- Poetrodjojo H., D’Agostino J. J., Groves B., Kewley L., Ho I. T., Rich J., Madore B. F., Seibert M., 2019, *MNRAS*, **487**, 79
- Portinari L., Chiosi C., Bressan A., 1998, *A&A*, **334**, 505
- Prochaska J. X., et al., 2017, *ApJ*, **837**, 169
- Péroux C., Howk J. C., 2020, *Annual Review of Astronomy and Astrophysics*, **58**, null
- Salim S., et al., 2007, *ApJS*, **173**, 267
- Sánchez-Menguiano L., et al., 2016, *A&A*, **587**, A70
- Sánchez S. F., et al., 2014, *A&A*, **563**, A49
- Sanders R. L., Shapley A. E., Zhang K., Yan R., 2017, *ApJ*, **850**, 136
- Sanders R. L., et al., 2020, arXiv e-prints, [p. arXiv:2009.07292](https://arxiv.org/abs/2009.07292)
- Schady P., Eldridge J. J., Anderson J., Chen T. W., Galbany L., Kuncarayakti H., Xiao L., 2019, *MNRAS*, **490**, 4515
- Shivaei I., et al., 2016, *ApJ*, **820**, L23
- Simionescu A., et al., 2019, *MNRAS*, **483**, 1701
- Smartt S. J., 2015, *Publ. Astron. Soc. Australia*, **32**, e016
- Somerville R. S., Davé R., 2015, *ARA&A*, **53**, 51
- Somerville R. S., Popping G., Trager S. C., 2015, *MNRAS*, **453**, 4337
- Springel V., White S. D. M., Tormen G., Kauffmann G., 2001, *MNRAS*, **328**, 726
- Springel V., White S. D. M., Jenkins A., et al., 2005, *Nature*, **435**, 629
- Stott J. P., et al., 2014, *MNRAS*, **443**, 2695
- Strickland D. K., Heckman T. M., Colbert E. J. M., Hoopes C. G., Weaver K. A., 2004, *ApJ*, **606**, 829
- Strom A. L., Steidel C. C., Rudie G. C., Trainor R. F., Pettini M., 2018, *ApJ*, **868**, 117
- Thielemann F. K., et al., 2003, in Hillebrandt W., Leibundgut B., eds, *From Twilight to Highlight: The Physics of Supernovae*. p. 331, [doi:10.1007/10828549_46](https://doi.org/10.1007/10828549_46)
- Tissera P. B., Rosas-Guevara Y., Bower R. G., Crain R. A., del P Lagos C., Schaller M., Schaye J., Theuns T., 2019, *MNRAS*, **482**, 2208
- Torrey P., Vogelsberger M., Genel S., Sijacki D., Springel V., Hernquist L., 2014, *MNRAS*, **438**, 1985
- Torrey P., et al., 2019, *MNRAS*, **484**, 5587
- Troncoso P., et al., 2014, *A&A*, **563**, A58
- Tumlinson J., et al., 2011, *Science*, **334**, 948
- Tumlinson J., Peebles M. S., Werk J. K., 2017, *ARA&A*, **55**, 389
- Vincenzo F., Belfiore F., Maiolino R., Matteucci F., Ventura P., 2016, *MNRAS*, **458**, 3466
- Walch S., et al., 2015, *MNRAS*, **454**, 238
- Wang X., et al., 2020, *ApJ*, **900**, 183
- Werk J. K., Prochaska J. X., Thom C., Tumlinson J., Tripp T. M., O’Meara J. M., Meiring J. D., 2012, *ApJS*, **198**, 3
- Werner N., Mernier F., 2020, *Hot Atmospheres of Galaxies, Groups, and Clusters of Galaxies*. pp 279–310, [doi:10.1007/978-3-030-38509-5_10](https://doi.org/10.1007/978-3-030-38509-5_10)
- Westfall K. B., et al., 2019, *AJ*, **158**, 231
- Wilkinson D. M., Maraston C., Goddard D., Thomas D., Parikh T., 2017, *MNRAS*, **472**, 4297
- Wiseman P., Schady P., Bolmer J., Krühler T., Yates R. M., Greiner J., Fynbo J. P. U., 2017, *A&A*, **599**, A24
- Wotta C. B., Lehner N., Howk J. C., O’Meara J. M., Oppenheimer B. D., Cooksey K. L., 2019, *ApJ*, **872**, 81
- Yates R. M., Kauffmann G., 2014, *MNRAS*, **439**, 3817
- Yates R. M., Kauffmann G., Guo Q., 2012, *MNRAS*, **422**, 215
- Yates R. M., Henriques B., Thomas P. A., Kauffmann G., Johansson J., White S. D. M., 2013, *MNRAS*, **435**, 3500
- Yates R. M., Thomas P. A., Henriques B. M. B., 2017, *MNRAS*, **464**, 3169
- Yates R. M., Schady P., Chen T. W., Schweyer T., Wiseman P., 2020, *A&A*, **634**, A107
- Zahid H. J., Dima G. I., Kudritzki R.-P., Kewley L. J., Geller M. J., Hwang H. S., Silverman J. D., Kashino D., 2014, *ApJ*, **791**, 130
- Zahid H. J., Kudritzki R.-P., Conroy C., Andrews B., Ho I.-T., 2017, *ApJ*, **847**, 18
- Zurita A., Florido E., Bresolin F., Pérez-Montero E., Pérez I., 2021a, *MNRAS*, **500**, 2359
- Zurita A., Florido E., Bresolin F., Pérez I., Pérez-Montero E., 2021b, *MNRAS*, **500**, 2380
- Zwaan M. A., Meyer M. J., Staveley-Smith L., Webster R. L., 2005, *MNRAS*, **359**, L30

This paper has been typeset from a \LaTeX file prepared by the author.